Phase formation, structure and properties of quaternary MAX phase thin films in the Cr-V-C-Al system: a combinatorial study

Chongchong Tang[a*], Michael Dürrschnabel[a], Ute Jäntsch[a], Michael Klimenkov[a], Martin Steinbrück[a], Sven Ulrich[a], Marcus Hans[b], Jochen M. Schneider[b], Michael Stüber[a]

[a]Institute for Applied Materials (IAM-AWP), Karlsruhe Institute of Technology (KIT), D-76021 Karlsruhe, Germany

[b]Materials Chemistry, RWTH Aachen University, D-52074 Aachen, Germany

[*]Corresponding author: chongchong.tang@kit.edu

Abstract

Tailoring of individual atomic layers via alloying to synthesize quaternary MAX phases allows for expanding their chemical diversity and fine-tuning of their properties. In this study, Cr-V/C/Al multilayered precursors were deposited via combinatorial magnetron sputtering, creating nanostructured architectures with periodic stacking of nanolayers and varying Cr:V ratios. Their phase transformation and underlying reaction mechanisms during subsequent thermal annealing in argon towards the prospective quaternary solid solution $(CrV)_{n+1}AlC_n$ MAX phases formation was systematically studied. Crystallization of $(CrV)_2AlC$ starts at approximately 500°C, while growth of higher-ordered $(CrV)_4AlC_3$ is observed from 960°C. Notably, intergrowth of $(CrV)_2AlC$ and $(CrV)_4AlC_3$ structures with coherent interface suggests that $(CrV)_2AlC$ acts as template for nucleation of $(CrV)_4AlC_3$. Thermal stability and high-temperature oxidation tests found that $(CrV)_2AlC$ exhibits higher thermal stability compared to $(CrV)_4AlC_3$ and films with $Cr_{72.7}V_{27.3}$ displayed good oxidation resistance at 1000°C, forming a protective bilayer oxide scale consisting of $(Cr,Al)_2O_3$ and Al_2O_3.

Key words: Quaternary MAX phases; Cr-V-C-Al system; Nanostructured multilayers; Combinatorial approach

1. Introduction

The demand for significantly enhancing the efficiency and reliability of technological processes in modern industries has led to a continuous need for innovative and advanced materials with complex property profiles [1,2]. One crucial requirement is the simultaneous presence of excellent high-temperature mechanical properties, such as high strength and toughness, along with oxidation resistance. A class of materials that shows great potential in meeting these demands are atomically layered carbide and nitride compounds, known as $M_{n+1}AX_n$ (MAX) phases, where M represents a transition metal, A stands for a mainly A-group element, and X is either carbon or nitrogen, with n typically ranging from 1 to 3 [3–6]. MAX phase compounds exhibit a hexagonal crystal structure with *$P6_3/mmc$* symmetry. Their crystal structures consist of twinned $M_{n+1}X_n$ slabs comprising edge-sharing M_6X octahedra, which are interleaved with atomic layers of the A element [4]. The different n values specify the number of the transition metal layers separating the A elemental layer. The covalent-ionic M-X bonds in the MAX phases are exceptionally strong and are comparable to their binary MX counterparts (for instance Ti-C bond energies in Ti_2AlC MAX phase and TiC are 2.61 eV and 2.56 eV, respectively); the metallic M-A bonds are relatively weak (Ti-Al bond energy in Ti_2AlC is 0.98 eV) [4,7]. Consequently, they exhibit unique physical, chemical, and mechanical properties originating from their layered crystal structures and special bonding characteristics. Generally, MAX phase compounds exhibit low density, excellent high-temperature mechanical properties, and low thermal expansion coefficients. Unlike conventional binary carbide or nitride ceramics, they are soft and readily machinable, reveal high thermal and electrical conductivities, as well as good thermal shock and damage tolerance.

One common route to tune materials' elemental constitutions and properties is through alloying. Tailoring of individual atomic layers via multi-element alloying to synthesize quaternary (and higher multi-element) MAX phases are attracting unprecedented interest with the recent discovery of new solid solution, ordered and sub-lattice high-entropy MAX phases [8–14]. The multi-element alloying strategy offers further degrees of compositional and structural control to increase their chemical versatility and expand their physical and chemical properties. Different alloying strategies have been demonstrated to, for example, introduce magnetic characteristics (e.g. alloying with Mn, Fe) [15,16], tune thermal expansion coefficients [17,18], and enhance oxidation resistance [19], of specific MAX phase materials. Exploring the quaternary systems within the materials design additionally will qualify to synthesize new thermodynamically stable quaternary MAX phase compounds whereas their ternary counterparts are thermodynamically unstable [20]. Recent studies revealed that other classes of elements, such as rare-earth elements [21] and noble metals [22], can be incorporated into ternary structures forming novel quaternary MAX phases; this offers additional prospects for tailoring properties and novel functionalities.

In the Cr-V-C-Al quaternary system, dual-transition metal solid solution MAX phases with three different structures $(CrV)_2AlC$, $(CrV)_3AlC_2$, and $(CrV)_4AlC_3$ have been experimentally demonstrated in bulk form [23–25]. MAX phases in this system are of particular interest since their ternary end members Cr_2AlC and V_2AlC exhibit supplementary exceptional properties apart from the common properties shared by many MAX phases. To be more specific, Cr_2AlC demonstrates excellent high-temperature oxidation and corrosion resistance, making it a promising material for protective coatings in harsh environments [26–28]. On the other hand, V_2AlC shows potential as electric contact due to its low resistivity [29]. Therefore, alloying

these ternary end members with each other to form solid solution $(CrV)_{n+1}AlC_n$ MAX phases, with different n values, offers vast possibilities to tailor their mechanical and physical properties while preserving certain favorable features for various advanced technological applications. While recently intensive studies have been conducted on quaternary $(CrV)_{n+1}AlC_n$ MAX phases, the focus has primarily been on theoretical exploration, experimental verification and properties evaluation of bulk products rather than thin films [24,25]. Reports on quaternary $(CrV)_{n+1}AlC_n$ thin films are very scarce; for instance Scabarozi addressed the deposition of $(Cr_xV_{1-x})_2AlC$ thin films through magnetron co-sputtering on sapphire at 850°C using four elemental targets and studied electric and magnetic properties of these films [30]. In the course of this research, Scabarozi reported the growth of higher-ordered $(Cr_xV_{1-x})_4AlC_3$ in two distinct compositional regions, indicating its potential phase stability depending on the film stoichiometry.

Our previous research demonstrated that thermal annealing of multilayered precursors, consisting of M/C/Al nanoscale sublayers, provides a facile method to synthesize phase-pure ternary MAX phase carbide films on various substrate materials [31,32]. In this study, we extended this method to the quaternary Cr-V-C-Al system and deposited Cr-V/C/Al multilayered thin film precursors by magnetron sputtering using one segmented Cr-V target, along with graphite and Al element targets. Utilizing a segmented Cr-V target enables deposition of the multilayered precursors with varying concentrations of chromium (Cr) and vanadium (V) of the Cr-V layers simultaneously, i.e. following a combinatorial thin film synthesis approach. This combinatorial approach enables an efficient exploration of the relationship between chemical composition and phase formation, particularly when the general stoichiometric ratio of the films changes [33]. The phase formation and transformation, as well as reaction mechanisms governing the prospective growth of quaternary $(CrV)_{n+1}AlC_n$ MAX phases during subsequent thermal annealing of the multilayered precursors, were comprehensively investigated. These investigations involved in-situ high-temperature X-ray diffraction (XRD) to monitor the phase changes during annealing, ex-situ XRD after cyclic annealing to further analyze the evolution of phase formation, and high-resolution transmission electron microscopy (HR-TEM) and atom probe tomography (APT) to gain detailed insights into their microstructure and local composition. Furthermore, thermal stability of the MAX phase thin films at high temperatures, their mechanical properties by microindentation, and high-temperature oxidation behavior in steam were evaluated. This study aims to contribute to and advance the understanding of synthesizing quaternary solid solution $(CrV)_{n+1}AlC_n$ MAX phase thin films from multilayered precursors and to identify the most suitable composition for phase formation and specific applications.

2. Experimental

The Cr-V/C/Al multilayered precursors were deposited by magnetron sputtering following a combinational approach using one segmented Cr-V target, along with graphite and Al element targets (all 75 mm diameter), as schematically illustrated in Fig. 1. An appropriate shutter system has been employed to regulate the deposition process, ensuring that only one specific target can contribute to film deposition at any given time. Six substrate samples were placed in a line in front of the segmented target. Consequently, thin film precursors with compositions ranging from Cr-rich to V-rich of the Cr-V layers can be obtained simultaneously. Two different types of substrates were utilized, i.e. Si wafer with thermally grown amorphous SiO_2 layer (for compositional analyses) and polished polycrystalline Al_2O_3 (for annealing, mechanical properties, and oxidation studies). Both types of substrates had a square shape, measuring 10 × 10 mm. The substrates were ultrasonically cleaned in an acetone bath for 10 minutes and sputter cleaned for 15 minutes in an argon plasma (pressure: 0.5 Pa) powered with radio frequency 500 W inside the deposition chamber before film deposition. The deposition process began with the chamber evacuated to a base pressure of approximately 1×10^{-4} Pa. Throughout the deposition, the working pressure of Ar was maintained at 0.5 Pa, and the targets were powered at 200 W for Cr-V and C, 120 W for Al (direct current for Cr-V and Al, and radio frequency for C). Notably, the substrates were not intentionally heated and were kept at ground potential during the entire deposition process.

To fabricate the desired multilayered structure of the precursors, a stop-and-go approach for the shutter and substrate holder movement was utilized during the top-down sputtering process (Fig.1). Inside the deposition chamber, both the substrate holder and the shutter were rotated to alternate between different targets. In such specific setup, the shutter possesses a significantly faster movement speed compared to the substrate holder. This speed difference translates to the shutter positioning itself over the target material before the substrate arrives. Subsequently, the substrate holder slowly moves beneath the target and shutter for a predetermined time. Notably, the deposition time for each position (from Cr-rich side CrV01 to V-rich side CrV06) progressively decreases as the substrate holder traverses from its initial contact with the plasma plume to its final position directly under the target. This time difference is approximately 4 seconds. This sequential deposition process provides the means to regulate the thickness of individual sublayers by adjusting the dwell time of substrates remained under each specific target. The total thickness of individual sublayers is ultimately determined by two factors: 1) substrate holder movement period, and 2) substrate holding time under a particular target. The designated thicknesses of each sublayer would be targeted as follows: approximately 15 nm for Cr-V, 5 nm for C, and 10 nm for Al. These thicknesses are chosen to achieve a precursor stoichiometry close to a 2:1:1 ratio, i.e., relevant to form a single-phase 211 MAX phase afterwards in thermal annealing of the precursors. This situation however cannot be precisely achieved for the above-described sputtering conditions. It is essential to note that variations in the sublayer thickness exist for each substrate at different positions due to various combined effects, primarily including different sputter yields of Cr and V, different angular distribution of the sputtered species and rotation of the shutters and substrates as previously described.

It is therefore anticipated that fluctuations in the Cr:V ratios and different sublayer thicknesses will result in varying overall stoichiometry of the multilayered precursors in different sample positions. To achieve the intended 211 condition (or any other pre-condition, for example 413) in all substrate positions, the target power and deposition time applied to the segmented Cr-V target has to be modified, according to the deposition rate of the Cr-V thin films at the individual position. Achieving a 2:1:1 stoichiometry across all substrate positions under the segmented Cr-V target simultaneously is inherently impossible due to the combined effects of the angular distribution of the sputtered species of different masses, the substrate holder movement, and the shutter operation during such combinatorial deposition. However, we focus in this manuscript on the multilayered films deposited under the above-specified parameters, as the consequences obtained for all samples, despite a clear deviation from the model cases, which significantly expedites the investigation of phase formation dependence on chemical composition. Two sets of thin film samples with different total thicknesses were deposited, a set of thinner films with ~1500 nm for annealing studies, and a set of thicker ones with ~4500 nm for mechanical properties and oxidation investigations. More information regarding the multilayer deposition utilizing a Leybold Z 550 sputter coater can be found in previous works [31,32].

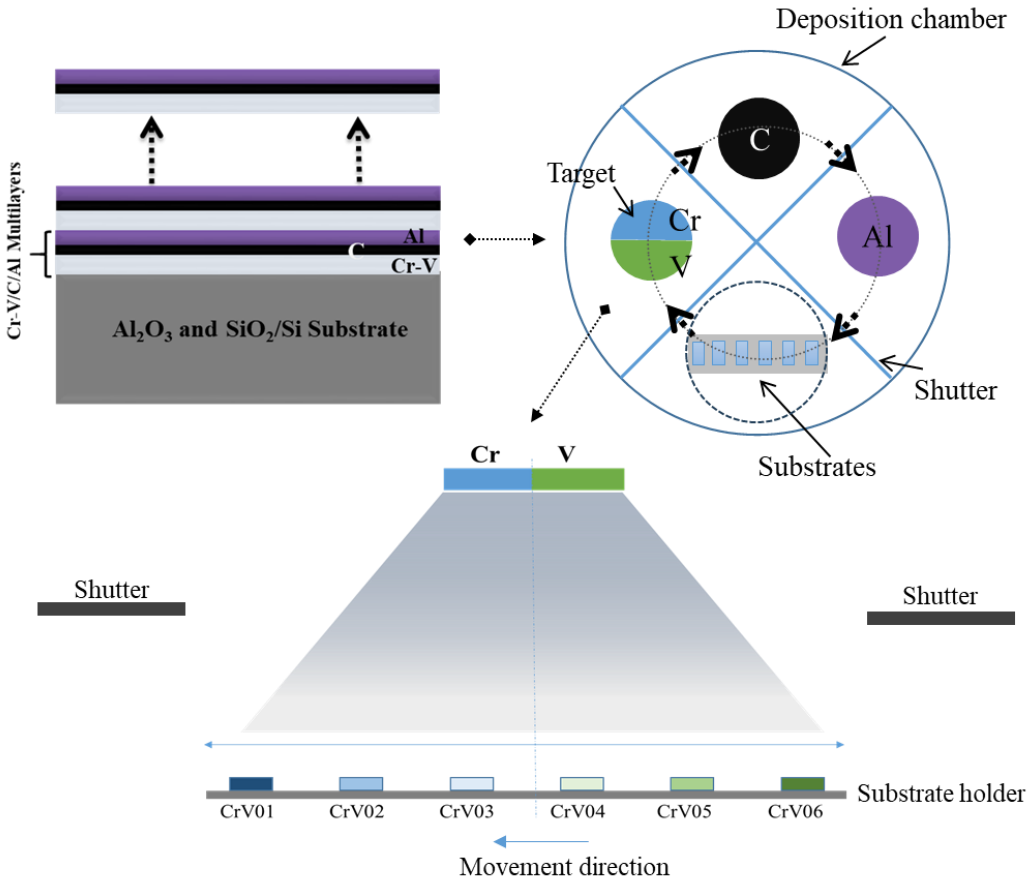

Fig. 1 Schematic illustration of magnetron-sputtering deposition of the Cr-V/C/Al multilayered precursors using a Cr-V segmented target and C and Al element targets in a combinatorial approach. Six substrate samples were placed in a line in front of the segmented target and films with compositions from Cr-rich to V-rich were deposited. The substrates were labeled as CrV01 to CrV06, from the Cr side to the V side.

The average chemical compositions of the as-deposited multilayered precursors were analyzed using electron probe microanalysis (EPMA) with a Cameca SX100 at 10 kV and 20 nA. The elemental depth profiles of one as-deposited multilayered precursor were measured using an Auger electron spectrometer (AES, PHI 680 Xi Auger Nanoprobe system). Their temperature-dependent phase formation was initially investigated by *in-situ* high-temperature X-ray diffraction (HT-XRD) analysis using an Anton Paar HTK 1200 N (Anton Paar GmbH) chamber. The temperature profile extended from 300°C to 1000°C with temperature steps of 20 K, applying a heating rate of 30 K/min between each step. XRD patterns were recorded using an Empyrean diffractometer (Malvern Panalytical) in Bragg-Brentano geometry (θ-2θ), with Cu Kα radiation (λ = 0.1540 nm) of 40 kV and 40 mA and 2θ ranging from 10° to 60°. During the measurement, an argon flow was used to purge the chamber, and the measuring time for each pattern was approximately 20 minutes. To compare and confirm their phase formation, the as-deposited multilayered precursors were also cyclically annealed in an argon atmosphere using a NETZSCH STA-449 F3 Jupiter thermal balance. During cyclic annealing experiments, a single, identical sample underwent a series of heating and cooling cycles. Each cycle involved heating the sample to a designated temperature with a dwell time of 10 minutes. A constant heating and cooling rate of 10 K/min was employed. Following cooling, the sample was transferred for XRD measurement. This process was iterated from 400°C to 1000°C, with a typical temperature increment of 50 or 100 K between cycles. Additionally, selected films were annealed at constant temperatures of 1000°C and 1200°C for different durations in an argon environment to study their temporal phase evolution and thermal stability at elevated temperatures. To minimize the residual oxygen content in the system and prevent significant oxidation of the films, an oxygen trapping system with a Zr oxygen getter was employed inside the furnace of the thermal balance.

The microstructure of selected annealed films was investigated using transmission electron microscopy (TEM) with a Thermo Scientific Talos F200X instrument, operating at an acceleration voltage of 200 kV. Cross-sectional TEM samples were prepared using the focused ion beam (FIB) technique and subsequently thinned through Ga ion milling at 30 kV inside a Zeiss Auriga workstation. Apart from TEM bright field, dark field, and high-resolution imaging, selected area electron diffraction (SAED) and energy dispersive X-ray spectroscopy (EDS) analyses were performed to scrutinize the local film area concerning grain structure and chemical compositions. The 3D chemical composition at the nanometer scale of selected films was investigated by laser-assisted atom probe tomography (APT) using a CAMECA LEAP 4000X HR instrument. For specimen preparation, FIB techniques were utilized in a FEI Helios Nanolab 660 dual-beam microscope following a standard protocol [34]. Microindentation was employed to evaluate the mechanical properties (hardness and Young's modulus) of the annealed films. This assessment was conducted using a CSM Micro Kombi Tester (Anton Paar GmbH) with a Vickers diamond tip in accordance with the Oliver and Pharr (OP) method [35]. During the indentation process, the depth was adjusted to be significantly larger than the surface roughness but simultaneously limited to one-tenth of the total film thickness to mitigate any potential substrate effects. For each sample, at least ten indentations were performed. The high-temperature oxidation behavior of three selected annealed films in steam at 1000°C was examined using the NETZSCH STA-449 thermal balance equipped with a steam furnace. The films were heated in argon atmosphere from room temperature to 1000°C with 10 K/min, and then steam was introduced into the furnace by a steam generator with 3 g/h H_2O. The oxidation time was set at 1 hour. After oxidation, the steam generator was switched off and the films were cooled in argon with 100 K/min

(natural cooling after around 800°C). After oxidation, the constitution, phase composition, microstructure and chemical composition of the oxide scale grown on the films were investigated by X-ray diffraction (XRD, Seifert PAD II diffractometer) and scanning electron microscopy (SEM, Philips XL30S) equipped with an energy dispersive X-ray spectroscopy (EDS) detector.

3. Results and discussion

3.1. Chemical composition and microstructure of the multilayered precursors

The average chemical composition of the as-deposited Cr-V/C/Al multilayered film precursors measured by EPMA and their related concentration ratios are shown in Table 1. As expected, for the films placed in front of the Cr side (starting with sample CrV01) to the V side (ending with sample CrV06), elemental compositions of the Cr-V layers from Cr-rich to V-rich were obtained. However, the Cr:V ratios do not show a symmetric distribution, with much higher Cr content in sample CrV01 (~72 at.%) than V content in sample CrV06 (~55 at.%), mainly because of higher sputtering yield of Cr than V under bombardment of particular noble gas ions [36]. In addition, the Cr and V concentrations and the corresponding Cr:V ratios display very close values for the samples CrV01 and CrV02, as well for the samples CrV05 and CrV06. This can be related to the angular distribution of the sputtered species in the plasma, the configuration of the magnetic field, and the geometrical arrangement of the samples in relation to the target [37]. The concentration of C gradually increased, while the content of Al decreased from the Cr-rich thin film CrV01 to the V-rich thin film CrV06. This difference arises from two major effects, i.e. substantially different deposition rates of Al and C at the specified deposition parameters (one magnitude higher for Al) and rotation of the substrate holder. The samples experienced different exposure on their travel path under the respective target, and the extended exposure of individual samples (particularly those underneath the Cr-side) during cycling accounted for higher percentages of total deposition time with respect to the Al target in relation to other two targets. Compared to other film precursors, the stoichiometry of sample CrV04 is closer to the 2:1:1 ratio, but with slightly higher Cr+V concentration than expected. Overall, the stoichiometry of all film precursors exhibits considerable deviation from any theoretically intended MAX-phase composition. In these thin film precursors, the (Cr+V):Al ratios range from 2.5 to 3.3, and the (Cr+V):C ratios change from 1.7 to 4.2. Oxygen and argon contaminations were detected within the films and their concentrations are generally pretty low (not shown in Table 1, please see Fig.2), below 2.0 at.% and 0.5 at.%, respectively.

The phase composition and local chemical composition of specific as-deposited films were examined using XRD and AES, respectively; corresponding results are presented in Fig.2. The broader XRD reflections in the angular range around 43.0° can be attributed to the transition metal sublayers, i.e. Cr-V, while the sharp reflections with higher diffraction intensities can be assigned with the polycrystalline alumina substrate (those reflections are marked by black square symbols). In the binary system Cr-V, both metals crystallize in body-centered cubic structure; Cr and V can form solid solutions over the entire

compositional range [38]. The diffraction peak locations of the Cr (110) plane (PDF card No. #06-0964) and the V (110) plane (PDF card No. #22-1085) are marked with dashed lines in Fig.2 (a). The broad, low intensity reflections at ~43.0° are located between those two reflections, which supports formation of nanocrystalline Cr-V solid solution phases. In addition, the position of these reflections shifted from ~43.8° of sample CrV01 to a lower angle ~42.7° of sample CrV05, consistent with the chemical composition measurements and lattice parameters of the two metallic phases (i.e., larger lattice parameters and smaller reflection angles for V compared to Cr). A faint and broad reflection at approximately 38.7° can be attributed to the Al (111) plane, but it is challenging to identify due to the high noise-to-signal ratio. The reflections from Al and C sublayers cannot be clearly resolved mainly due to their low thickness and amorphous structure, respectively, as confirmed by our previous studies [32].

The periodic arrangement of Cr-V, C, and Al sublayers in the as-deposited films is evident in the AES depth profiles. Fig.2 (b) shows exemplarily an AES depth profile for the CrV03 thin film sample, representative for all films. Across the analyzed layer thickness, a systematic and repeated sequence of the individual layers is identified, with clearly reproduced chemical gradients at the layer interfaces. The peak intensity of Cr coincides with that of V, supporting the claim of Cr and V co-deposition in the related sublayers. The film surface is rich in oxygen and contains both metals and some carbon. This can be attributed to formation of native oxides and hydrocarbon adsorbates on the surface when the films are exposed to the ambient atmosphere. The argon and oxygen contaminations of the film samples (in the bulk volume) measured by AES is very low, as displayed in Fig.2 (b), corresponding with the data obtained in the electron microprobe analyses. Consistent with our previous findings on ternary films [31], a quasi-periodic argon depth profile aligning with the periodic carbon depth profile as identified by AES measurement suggests that the Ar atoms are mainly enriched in the amorphous C layers.

Table 1 Average elemental composition of the as-deposited multilayered films measured by EPMA (at.%).

Nr.	C	Al	V	Cr	Cr:V	(CrV):Al	(CrV):C
CrV01	14.4	24.8	16.5	44.3	$Cr_{72.7}V_{27.3}$	2.5	4.2
CrV02	16.8	22.4	16.7	44.1	$Cr_{72.4}V_{27.6}$	2.7	3.6
CrV03	20.3	21.0	20.2	38.5	$Cr_{65.5}V_{34.5}$	2.8	2.9
CrV04	22.6	20.8	23.6	33.0	$Cr_{58.2}V_{41.8}$	2.7	2.5
CrV05	24.6	17.5	32.8	25.1	$Cr_{43.3}V_{56.7}$	3.3	2.4
CrV06	31.1	16.6	28.6	23.7	$Cr_{45.3}V_{54.7}$	3.1	1.7

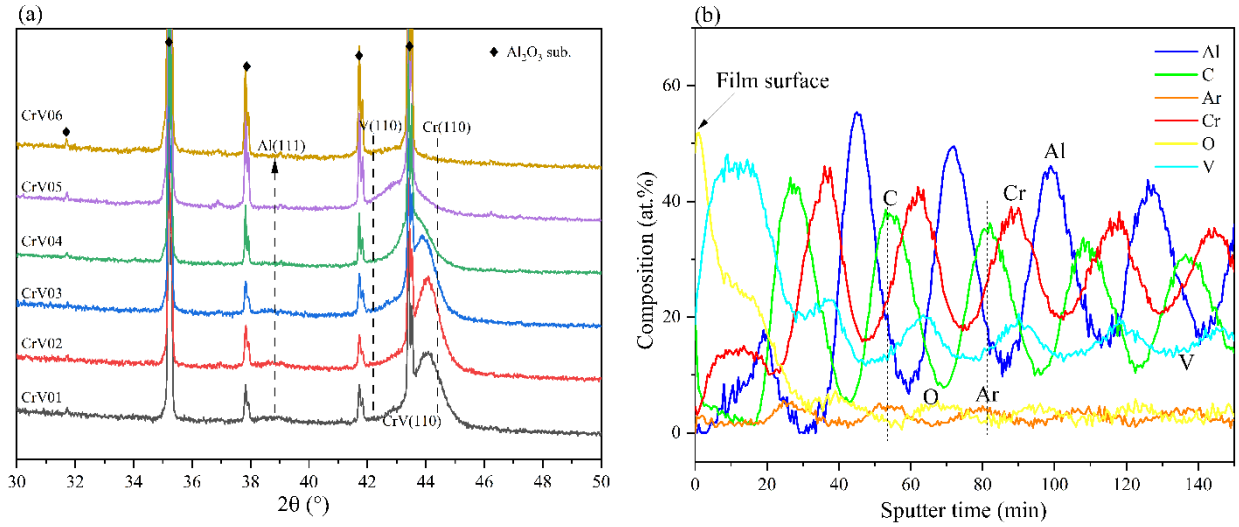

Fig. 2 Phase and chemical composition of the as-deposited multilayered precursors. (a) XRD patterns of all multilayered thin film precursors, (b) AES depth profile of the as-deposited thin film sample CrV03.

3.2. Phase transformation and microstructure formation during annealing

The as-deposited Cr-V/C/Al multilayered precursors were subject to thermal annealing in inert atmosphere (argon) and their thermally induced phase formation/transformation and microstructure evolution was initially investigated by *in-situ* HT-XRD. These analyses reveal that the phase formation depends not only on the chemical compositions of the individual film precursors but also on the annealing temperatures and holding times. Various quaternary solid solution MAX phases, $(CrV)_2AlC$ and $(CrV)_4AlC_3$, formed during annealing of the different multilayered precursors. The results can be classified into two different categories based on crystallization of these quaternary MAX phases: the first category includes thin film samples CrV01-CrV04 and CrV06, while the second category consists of only sample CrV05. More specifically, in the first category, the 211-structured quaternary solid solution $(CrV)_2AlC$ MAX phase was the only MAX phase detected during the HT-XRD measurements up to 1000°C, while in the second category, the $(CrV)_4AlC_3$ MAX phase with higher-ordered 413 structure crystallized at annealing temperature reaching about 960°C. The XRD patterns for thin films of the two different categories are exemplarily displayed in Fig.3 for sample CrV01 and sample CrV05, respectively.

No apparent new phase formation was recognized in both thin films with the annealing temperature increasing from 300°C up to ~600°C, and the CrV(110) reflection shows decreasing intensity in this temperature range. However, mutual diffusion and intermixing occur within the nanoscale multilayers and some amorphous structures or nanocrystalline phases may be formed in this temperature range [31,39]. When the annealing temperature reaches 600°C, two broad reflections appear in both diffractograms, located at diffraction angles ~13.6° and 41.6°. These two reflections clearly indicate that nucleation and crystallization of the quaternary solid solution $(CrV)_2AlC$ MAX phase happens at temperatures between 500°C and 600°C. This is concluded with respect to the theoretical positions of the specific reflections of the (002) and (006) planes of the quaternary $(CrV)_2AlC$ MAX phase. Such crystallization onset behavior was observed in the same temperature range similarly for ternary Cr_2AlC

(PDF card No. #29-0017) and V_2AlC (PDF card No. #29-0101) MAX phases [40] synthesized from nanoscale multilayered thin film precursors using the same approach as here [31,32]. Regarding the Cr-rich thin film CrV01, no additional reflections that can be assigned to the 211 MAX phase were detected as the annealing temperature further increases, Fig.3 (a). The intensities of these two reflections gradually increase, and the diffraction peaks become more symmetric and narrower, and shift as well to lower angles (owing to thermal expansion with increasing temperatures). In contrast, the XRD patterns of the V-rich thin film CrV05 showed the appearance of further, different reflections with increasing temperature: one diffraction reflection centered at ~40° was observed from about 800°C, and two further diffraction reflections located at ~15.5° and 39.6° were detected from about 960°C. The first reflection can be attributed to the (102) lattice plane of $(CrV)_2AlC$, while the latter two reflections are assigned to the growth of the higher-ordered $(CrV)_4AlC_3$ MAX phase, indicated by their (004) and (0010) planes (verified by additional XRD and TEM analyses, see sections 3.3 and 3.4). Growth of chromium carbides (Cr_7C_3 and Cr_3C_2, PDF card number Cr_7C_3 #36-1482, Cr_3C_2 #35-0804) as secondary phases was observed in both films. Subsequent TEM and APT analyses (Section 3.4) revealed the incorporation of approximately 10 at.% V into the chromium carbide phases. This observation aligns with prior thermodynamic evaluations, which predicted a vanadium solubility of up to 15 at.% in these chromium carbides at 1000°C [41]. To reflect this information, the designation of these phases has been revised in later sections to M_7C_3 and M_3C_2 (or M_xC_y), where M represents a combination of chromium (Cr) and vanadium (V) atoms. Their diffraction peaks appear from around ~920°C and are marked by arrows in Fig.3 (b). The observed lower intensity and presence of noisy features in the HT-XRD patterns in Fig.3 can be attributed to weaker X-ray signal (window configuration) and faster scans (needed for high-temperature dynamics).

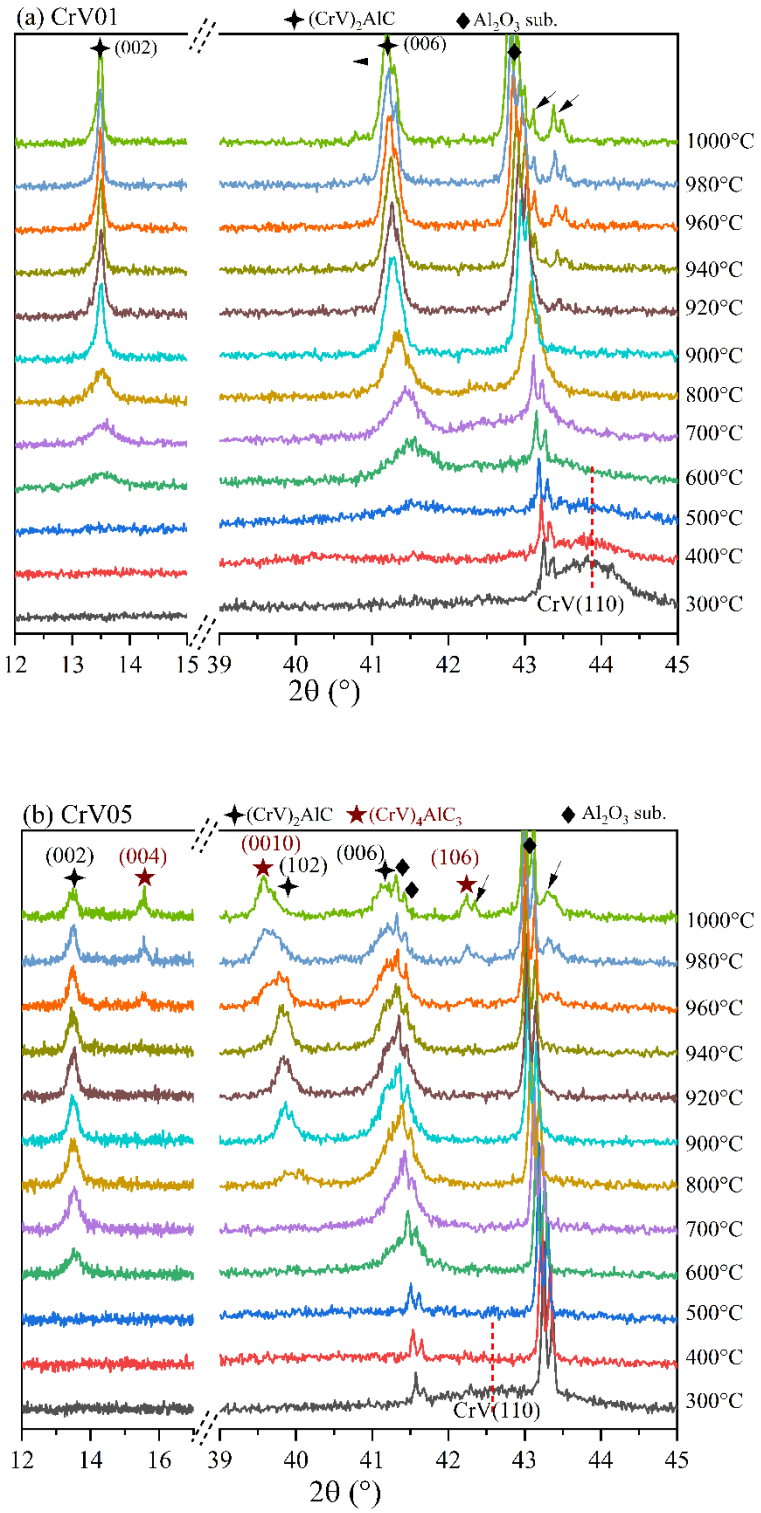

Fig. 3 Selected in-situ HT-XRD patterns of two multilayered precursors annealed from 300 to 1000°C with a temperature step of 20 K. (a) Cr-rich thin film CrV01, and, (b) V-rich thin film CrV05. The annealing time for each temperature step was approximately 20 mins. The diffraction peaks marked by arrows are attributed to M_7C_3 and M_3C_2 (M: Cr and V) phases.

To verify the temperature-dependent phase formation and growth of the higher-ordered $(CrV)_4AlC_3$ MAX phase in the V-rich thin film CrV05, all Cr-V/C/Al multilayered thin film precursors were also subjected to cyclic annealing up to 1000°C in argon. Fig.4 shows the XRD patterns of CrV01 and CrV05 samples after annealing from 400°C to 1000°C as examples. In addition, comparisons of the reflections at low 2θ ranges for all thin films after annealing at 800°C and 1000°C are displayed in Fig.5 (XRD patterns of full 2θ ranges are given in Fig.S1). Compared to the as-deposited films, a broad hump of very low intensity located at ~40° evolves after annealing at 400°C and 450°C, as displayed in Fig.4. In this angular position, one could expect the formation of an intermediate product of disordered $(M,Al)_2C_x$ (M: Cr and V) carbide phase before crystallization of MAX phase. Phase transition from such disordered carbide phase to ordered ternary MAX phases has been reported to take place with increasing annealing temperature [42–44]. This phase could not be noticeably acquired during the HT-XRD measurements, most probably due to its nanocrystalline feature, relatively short probe time and low signal-to-noise ratio in the HT-XRD analyses. Crystallization of the solid solution quaternary $(CrV)_2AlC$ MAX phase was observed for both thin films after annealing at 500°C, as indicated by appearance of the specific (002) diffraction peak of this phase at ~13.5° in Fig.4 (marked by a dashed, red-colored circle). More diffraction reflections attributed to the $(CrV)_2AlC$ MAX phase appeared with increasing annealing temperature and these diffraction peaks become sharper and narrower, indicating enhanced degree of crystallinity. In addition, the acquired reflections primarily from the (00l) lattice planes indicate that the $(CrV)_2AlC$ crystallites have a basal plane preferred orientation.

Formation of the higher-ordered $(CrV)_4AlC_3$ MAX phase was only identified in case of the V-rich thin film CrV05 after annealing at 1000°C, as revealed in both Fig.4 and Fig.5. The stacked diffraction patterns after annealing at 800°C in Fig.5 (a) explicitly reveal that the reflections of the (002) plane from the crystalline MAX phase of all thin films are located in between those of ternary V_2AlC and Cr_2AlC MAX phases, which supports the formation of quaternary solid solution $(CrV)_2AlC$ MAX phase. Compared with the Cr-rich thin film CrV01, the (002) diffraction peak of the V-rich thin film CrV06 shifts slightly toward lower 2θ angles, closer to the peak position of V_2AlC (002). The diffraction peak centered at ~15.8° in Fig.5 (b), which was detected only in CrV05 after annealing at 1000°C, can be indexed to the (004) plane of the solid solution $(CrV)_4AlC_3$ MAX phase. Compared to ternary V_4AlC_3 (004) (PDF card No. #16-3549), its position shifts to a higher 2θ angle because of incorporation of Cr into the transition metal sublattice. M_7C_3 and M_3C_2 (M: Cr and V) phases are observed as secondary phases in these two films; their diffraction peaks appear when the annealing temperature reaches and surpasses ~900°C. In addition, diffraction signals with relatively low intensity from an intermetallic compound Cr_2Al were found for the Cr rich thin films CrV01 and CrV02 after annealing at 1000°C (Fig.S1). Therefore, the remaining materials within the films, excluding the formation of MAX phases, crystallize into these impurity phases after annealing at relatively high temperatures. Their absence at lower annealing temperatures (600-800°C) can be explained by their low volume fraction and poor crystallinity at low temperatures. Considering these films are Cr-rich, it can be expected that M_7C_3 and Cr_2Al are the two secondary phases forming in films with higher Al content, while the secondary phases are M_7C_3 and M_3C_2 carbides only in films with lower Al content. The phase formations are in good agreement with phase equilibrium predicted by the Cr-C-Al ternary phase diagram assuming that V atoms are predominantly incorporated into the quaternary solid solution $(CrV)_2AlC$ MAX phase (Fig.S2 with inserted symbols representing thin film stoichiometry). It is anticipated that phase-pure $(CrV)_2AlC$ thin films can be synthesized if the film stoichiometry aligns well with the desired 2:1:1 ratio.

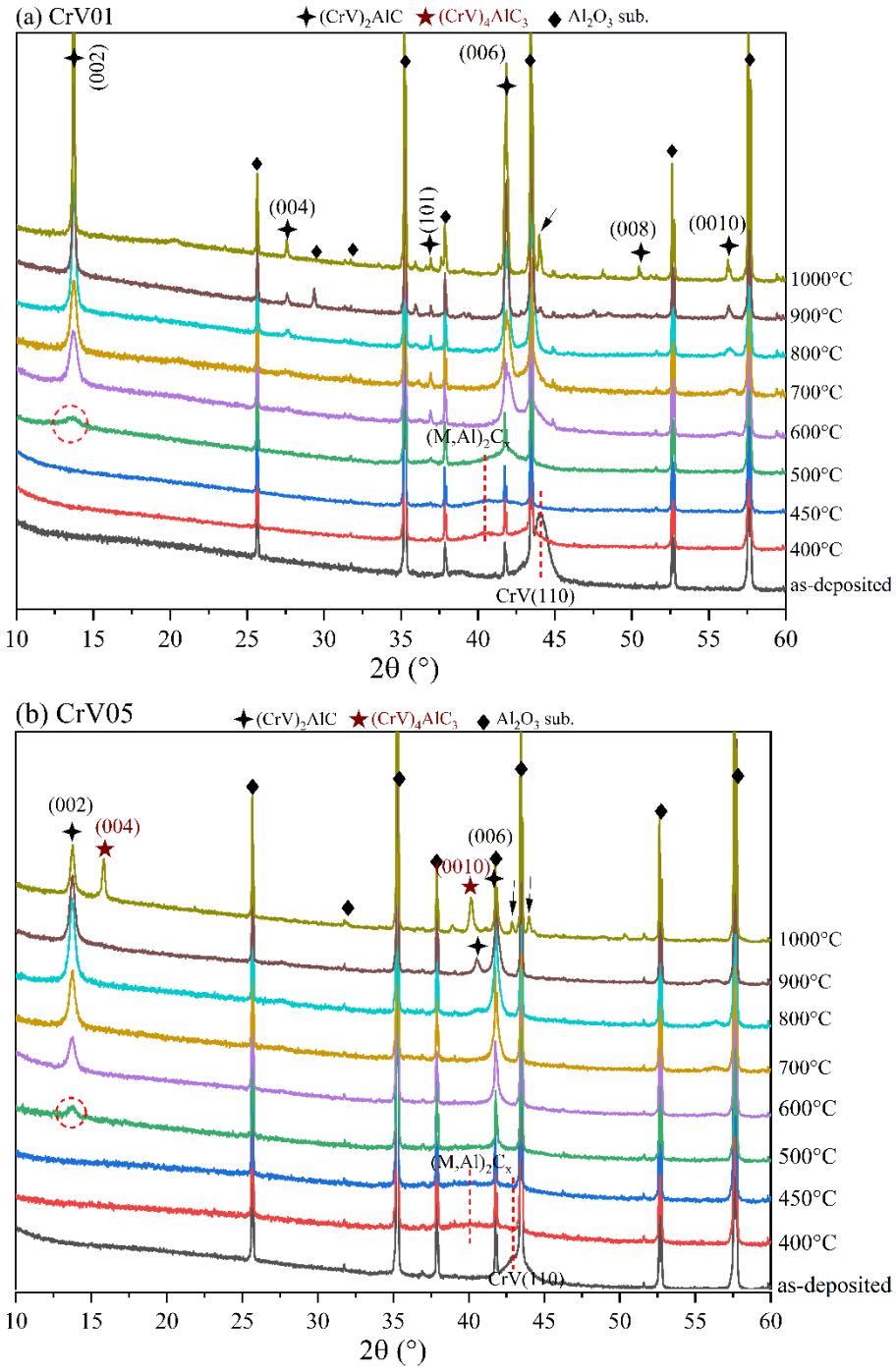

Fig. 4 XRD patterns of two multilayered film precursors after cyclic annealing at different temperatures in argon from 400°C to 1000°C. (a) CrV01 and (b) CrV05. The annealing time at each temperature was 10 mins. The diffraction peaks marked by arrows are attributed to M_7C_3 and M_3C_2 (M: Cr and V) phases.

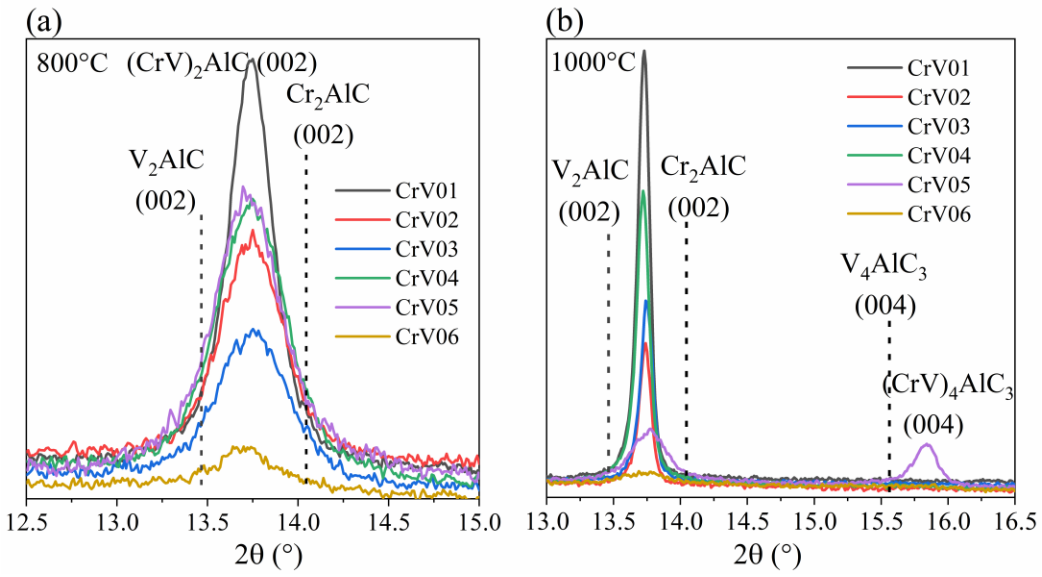

Fig. 5 XRD patterns at low 2θ of all multilayered film precursors after annealing at the same temperature in argon. (a) 800°C, and (b) 1000°C. The annealing time at each temperature was 10 mins. Peak positions of ternary V_2AlC, Cr_2AlC, and V_4AlC_3 MAX phases are shown for comparison.

The lattice parameters *a* and *c* of the solid solution $(CrV)_2AlC$ MAX phase after annealing at 800°C have been derived from the XRD patterns, and are plotted in Fig.6 including values of ternary Cr_2AlC and V_2AlC for comparison. Obviously, their lattice parameters lie between those of ternary Cr_2AlC and V_2AlC, but do not follow a linear relationship from the Cr-rich sample CrV01 to the V-rich sample CrV06. The values first decrease slightly from sample CrV01 to sample CrV03, then increase progressively from sample CrV04 to sample CrV06. Previous studies on bulk materials showed that the lattice parameters of solid solution $(CrV)_2AlC$ and $(CrV)_4AlC_3$ obey the Vegard's law, i.e. the lattice parameters increase linearly with increasing V-content [17]. Following Vegard's law, the estimated Cr concentration (Cr/(Cr+V)) in $(CrV)_2AlC$ ranges from ~80 at.% in CrV03 to ~45 at.% in CrV06. The variation of Cr:V ratios in the $(CrV)_2AlC$ phase is conceivably linked to the initial film stoichiometry and growth of secondary phases. Nevertheless, higher V content in the solid solution $(CrV)_2AlC$ MAX phase can be confirmed for films near the V-target side.

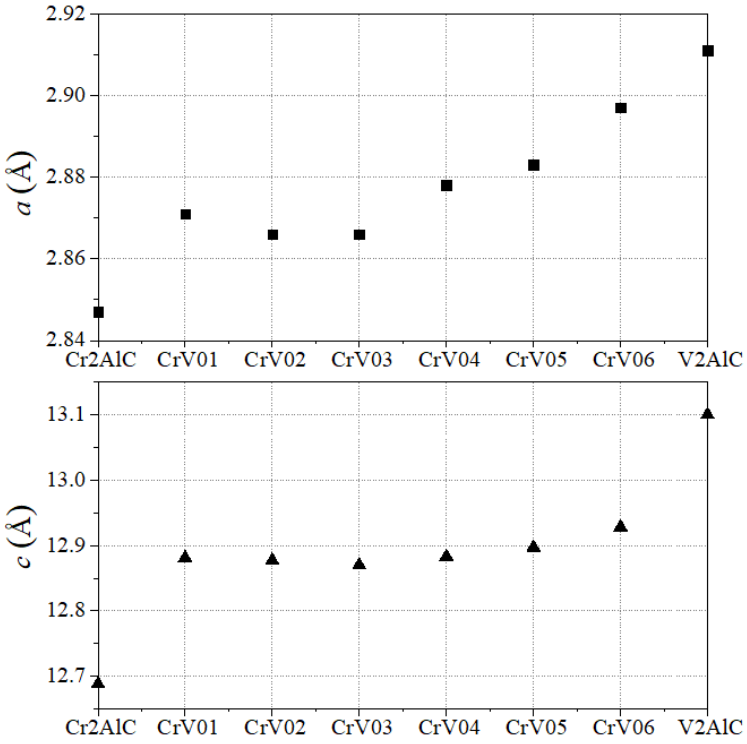

Fig. 6 Lattice parameters of the $(CrV)_2AlC$ MAX phase based on XRD patterns of the film precursors after annealing at 800°C for 10 min. Data for ternary Cr_2AlC and V_2AlC are included for comparison.

3.3. Time-dependent phase formation and thermal stability

To gain a deeper insight into the formation mechanism of the higher-ordered $(CrV)_4AlC_3$ MAX phase in the V-rich sample CrV05, temporal phase evolution at 1000°C was traced by XRD after annealing for different times. Fig.7 (a) and (b) show the XRD patterns and relative diffraction intensity of $(CrV)_2AlC$ (002) and $(CrV)_4AlC_3$ (002) reflections after annealing from 1 to 120 min, respectively.

Crystallization of $(CrV)_4AlC_3$ was already noticed after 1 minute of annealing since its nucleation tempeature locates at around 960°C as revealed by HT-XRD (Fig.3 (b)), but the dominant phase identified initially was $(CrV)_2AlC$. The temporal phase evolution proceeds through essentially three stages based on the relative diffraction intensity of the two MAX phases, as indicated in Fig.7 (b). In Stage I, the relative diffraction intensity of $(CrV)_4AlC_3$ (002) increased rapidly, at the expense of $(CrV)_2AlC$ (002). It is suggested that the chemical composition of the remaining materials in sample CrV05 (Table 1) moves towards 413 stoichiometry after nucleation and crystallization of the lower-ordered $(CrV)_2AlC$ starting from lower temperatures. The lower-ordered $(CrV)_2AlC$ possibly will serve as nucleation template for the higher-ordered $(CrV)_4AlC_3$ since they have similar nanolaminated crystal structures (see TEM results in next section). Nucleation and growth of the $(CrV)_4AlC_3$ was initiated once the annealing temperature is high enough to overcome the energy barriers to form this higher-ordered structure. In Stage II, the relative

diffraction intensity value reached a plateau after ~20 min annealing. The growth of the $(CrV)_4AlC_3$ thus appears to be completed after annealing at 1000°C for 20 min. The $(CrV)_4AlC_3$ becomes the dominant MAX phase since the stoichiometry of the as-deposited multilayered precursors in sample CrV05 is closer to 413 than to 211 (according to data presented in Table 1, the stoichiometric ratio can be split into approximately 65% 413 and 35% 211). In Stage III, after more than 40 min of annealing time, the diffraction intensity of $(CrV)_4AlC_3$ gradually increases, while the intensity of $(CrV)_2AlC$ gradually decreases. This effect can be rationalized by the outward diffusion of aluminum from the film during long-term annealing, leading to partial decomposition of the MAX phase structures [45,46] and transformation of some $(CrV)_2AlC$ to the higher-ordered structure of $(CrV)_4AlC_3$ with lower Al content [17,47]. The Al concentration within the films was measured after annealing at three different times at 1000°C (Fig. S3), revealing gradual decrease from 16.1 at.% after 10 min to approximately 11.5 at.% after 120 min. This concentration level aligns close to the ideal Al content (12.5 at.%) in $(CrV)_4AlC_3$, which supports that the 413 MAX phase becomes the primary phase following annealing for 120 min. Additionally, isolated alumina particles were observed after this prolonged annealing period, providing further evidence of outward diffusion of Al (attracted by residual oxygen inside the annealing furnace). The substantially different slopes of the curves in Stages I and III indicate that the nucleation and growth of the MAX phases proceed with much faster kinetics than their decomposition dominated by outward diffusion of Al. To realize the controllable synthesis of crystalline $(CrV)_2AlC$ and $(CrV)_4AlC_3$ thin films with desirable and reproducible phase compositions and microstructures from the multilayered precursors, suitable annealing temperatures and durations combined with in-depth time-resolved and locally-resolved analyses are essential.

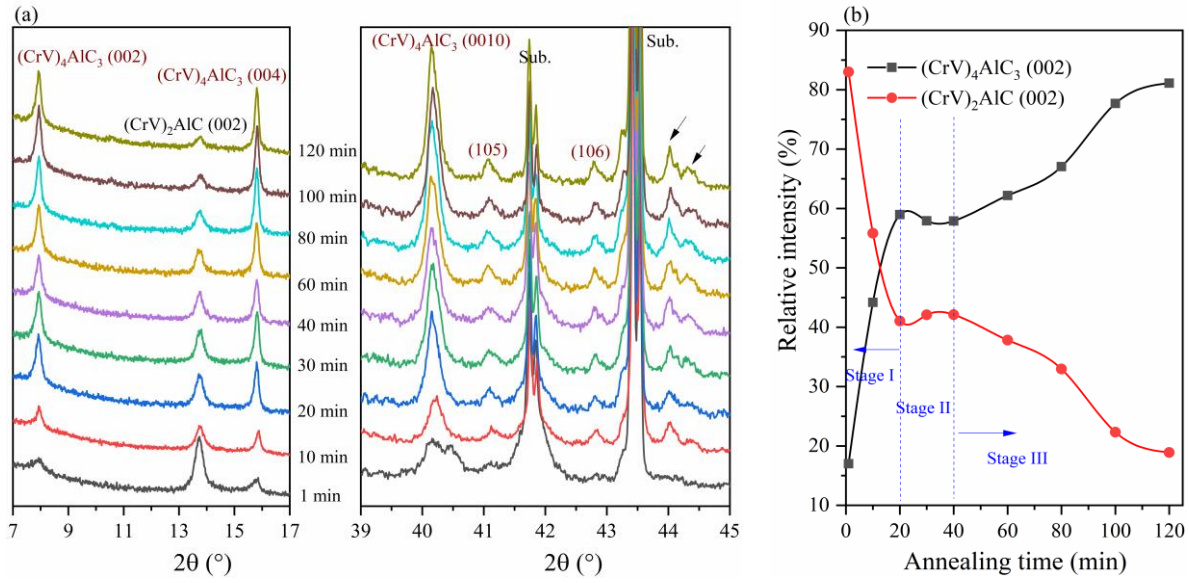

Fig. 7 Temporal phase evolution of the V-rich thin films CrV05 during annealing at 1000°C in argon from 1 min to 120 min. (a) XRD patterns, (b) Relative diffraction intensity of $(CrV)_4AlC_3$ (002) and $(CrV)_2AlC$ (002). The notation "Sub." represents the alumina substrate. The diffraction peaks marked by arrows are attributed to M_7C_3 and M_3C_2 (M: Cr and V) phases.

Thermal stability and associated decomposition mechanisms of $(CrV)_2AlC$ and $(CrV)_4AlC_3$ MAX phases were comparatively studied by annealing both Cr-rich and V-rich thin films (exemplarily CrV03 and CrV05 thin films samples) at higher temperature 1200°C in argon atmosphere. Phase evolution and microstructure changes were investigated by XRD analyses. The results are displayed in Fig.8 including also the XRD patterns of the samples after annealing at 1000°C and 1100°C for comparison. After annealing the Cr-rich sample CrV03 from 1000 to 1100°C, the diffraction intensity of $(CrV)_2AlC$ (002) lattice plane increased and its full width at half maximum (FWHM) diminished, indicating enhanced crystallinity at higher temperature. In contrast, gradually reduced diffraction intensity of the $(CrV)_2AlC$ (002) lattice plane was observed after annealing at 1200°C from 10 min to 80 min, which specifies partial decomposition of the MAX phase grains. In case of the V-rich thin film CrV05, both $(CrV)_2AlC$ and $(CrV)_4AlC_3$ represent the main phases after annealing at 1000°C, since the XRD reflections of $(CrV)_2AlC$ (002) and $(CrV)_4AlC_3$ (002)/(004) lattice planes show similar intensities (Fig.8 (b)). However, after annealing at 1100°C, reflection of the $(CrV)_2AlC$ (002) lattice plane was barely detectable while the diffraction intensities of the $(CrV)_4AlC_3$ (002)/(004) planes were amplified. During annealing at 1200°C, the diffraction intensities of the $(CrV)_4AlC_3$ (002)/(004) planes decreased rapidly and continuously with increasing annealing time, and their diffraction reflections cannot be detected after 80 min annealing. In the meantime, additional reflections from binary carbides (Cr_xC_y and VC_x) appeared and their diffraction intensity progressively enhanced with increasing annealing time, as demonstrated in Fig.8 (b). These findings are consistent with the results of Fig.7, i.e. the lower-ordered $(CrV)_2AlC$ can transform to the higher ordered $(CrV)_4AlC_3$ structure and the MAX phase structures will finally decompose to binary carbides because of Al loss during high temperature annealing.

For these two MAX phases, it is obvious that their thermal stability at elevated temperatures depends on their aluminum content and crystal structure. $(CrV)_2AlC$ with 25 at.% Al possesses good thermal stability at 1200°C in argon atmosphere and decomposes more slowly, while $(CrV)_4AlC_3$ containing only 12.5 at.% Al decomposes quickly. Similar behavior with different decomposition rate was also observed for MAX phases in the Ti-Al-N system in which Ti_4AlN_3 was reported to show faster decomposition rate than Ti_2AlN [47]. In addition, higher diffusion coefficient of Al atoms in higher-ordered MAX phase (Ti_3AlC_2) than in lower-ordered MAX phase (Ti_2AlC) were also experimentally measured in the Ti-Al-C system [48]. One possible explanation is that the shorter but stronger Al–M bonds in the 211 structure compared to those in the 312 and 413 structures make out-diffusion of Al more difficult. Generally, the weak metallic M-A bonds and strong covalent M-X bonds in the MAX phase structures make the A element highly mobile and promote its outward diffusion at elevated temperatures, either by forming an A-rich layer on the surface in oxidizing environments [27,49] or by volatilization under high vacuum conditions [45,47,50].

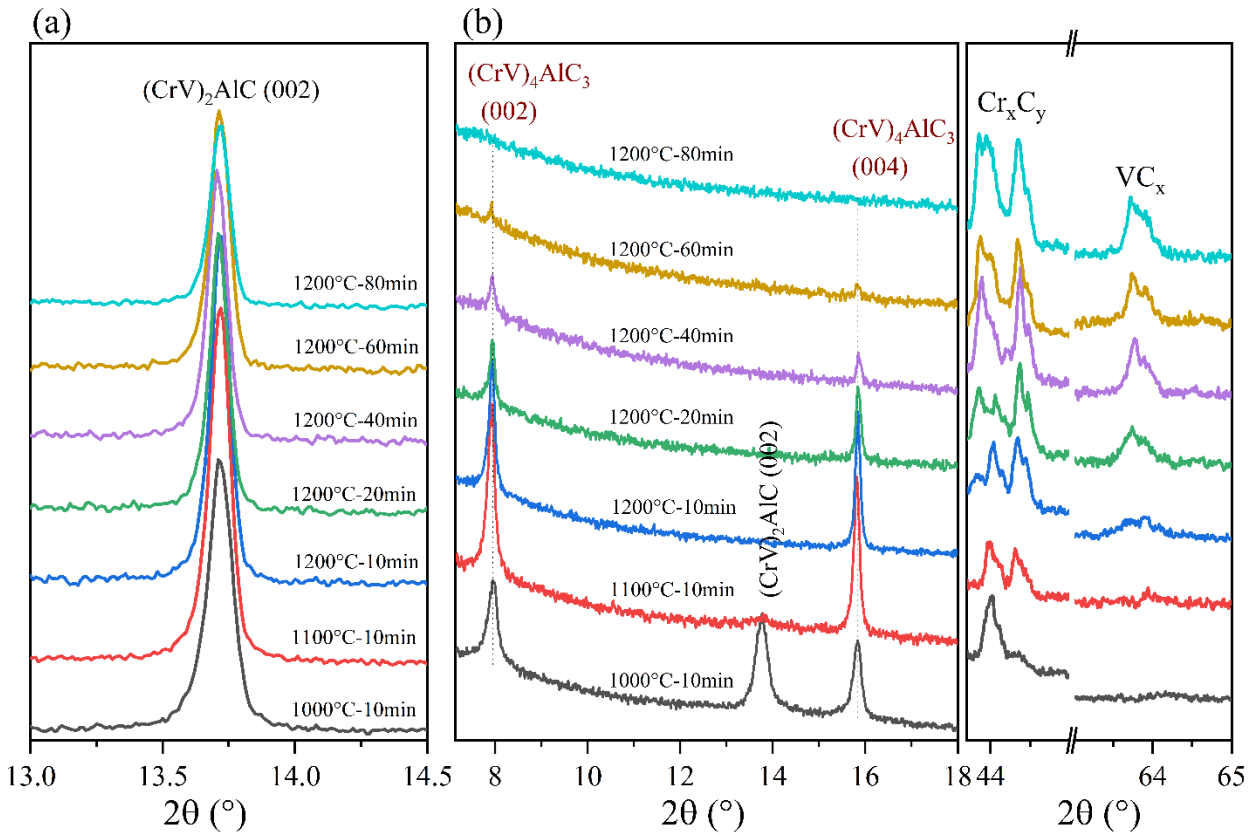

Fig. 8 Thermal stability of the thin films samples containing $(CrV)_2AlC$ and $(CrV)_4AlC_3$ MAX phases studied by XRD analyses during annealing at 1200°C in argon. (a) Cr-rich thin film CrV03, and, (b) V-rich thin film CrV05. XRD patterns after annealing at 1000°C and 1100°C are included for comparison.

3.4. Constitution and microstructure after annealing at 1000°C

The microstructure and phase constitution of the V-rich thin film CrV05 consisting of both $(CrV)_2AlC$ and $(CrV)_4AlC_3$ MAX phases after annealing at 1000°C were investigated by HR-TEM and APT. The results are shown in Figs. 9-11. Fig. 9 illustrates the high angle annular dark field (HAADF) and dark field (DF) STEM images, as well as the results of EDX mapping at low magnification. On the film surface, a thin Al_2O_3 layer with ~ 20 nm thickness decorated with some isolated Al_2O_3 particles beneath was identified (EDX mapping of O and Al). Growth of such thin Al_2O_3 layer can be attributed to exposure of the sample surface to the ambient atmosphere (oxygen adsorption) after deposition as well as to potentially residual air in the annealing furnace. This observation also supports the temporal phase evolution and thermal stability investigations that outward diffusion of Al at elevated temperatures accounts for the phase transition and final decomposition of the MAX phase structures.

Inside the annealed films, two different types of grains were identified with lamellar and granular morphology (marked in the EDX mapping of V and Cr). The lamellar-shaped grains are composed of all four elements but with variations in V concentration. HR-TEM analyses confirm that they are the two

different ordered MAX phases, i.e. $(CrV)_2AlC$ and $(CrV)_4AlC_3$ with different Cr:V ratios, consistent with XRD results. Some lamellar-shaped grains are tilted toward the film/substrate interface. The granular-shape grains consist of mainly Cr and C, with around 10 at.% V, and are indexed as V-doped chromium carbides M_7C_3 and/or M_3C_2 (M: Cr and V) by HR-TEM (Fig.S4). The particular lamellar shape of the MAX phase grains, which has been observed also in our previous studies of the ternary systems [31,32], is mainly related to the fact that the unique nanostructured architectures in the multilayered precursors permit the grains to grow rapidly in the transverse direction. The granular-shape of chromium carbide grains can be explained by their crystallization at higher temperatures from the remaining materials within the film after the crystallization of MAX phases. Some chromium carbide grains were found directly beneath the surface Al_2O_3 layer. These grains most probably originate from the decomposition of the MAX phase in the vicinity of the surface region after outward diffusion of Al. It is worth mentioning that precipitation of nanoscale Ar bubbles was observed inside the annealed thin film, which is evident from the EDX mapping of Ar. Preferential incorporation of Ar atoms into the amorphous carbon layers within the as-deposited multilayered precursors was observed before (Fig.2), similar to our previous studies in ternary V/C/Al multilayered films [31]. In the V/C/Al multilayered films after annealing at 800°C, the Ar bubbles displayed more periodical, layered distribution characteristics. However, the distribution of argon bubbles in the CrV05 film after 1000°C annealing here appears to be random. Higher annealing temperatures may promote the migration and coalescence of these nanoscale Ar bubbles, making their distribution more random.

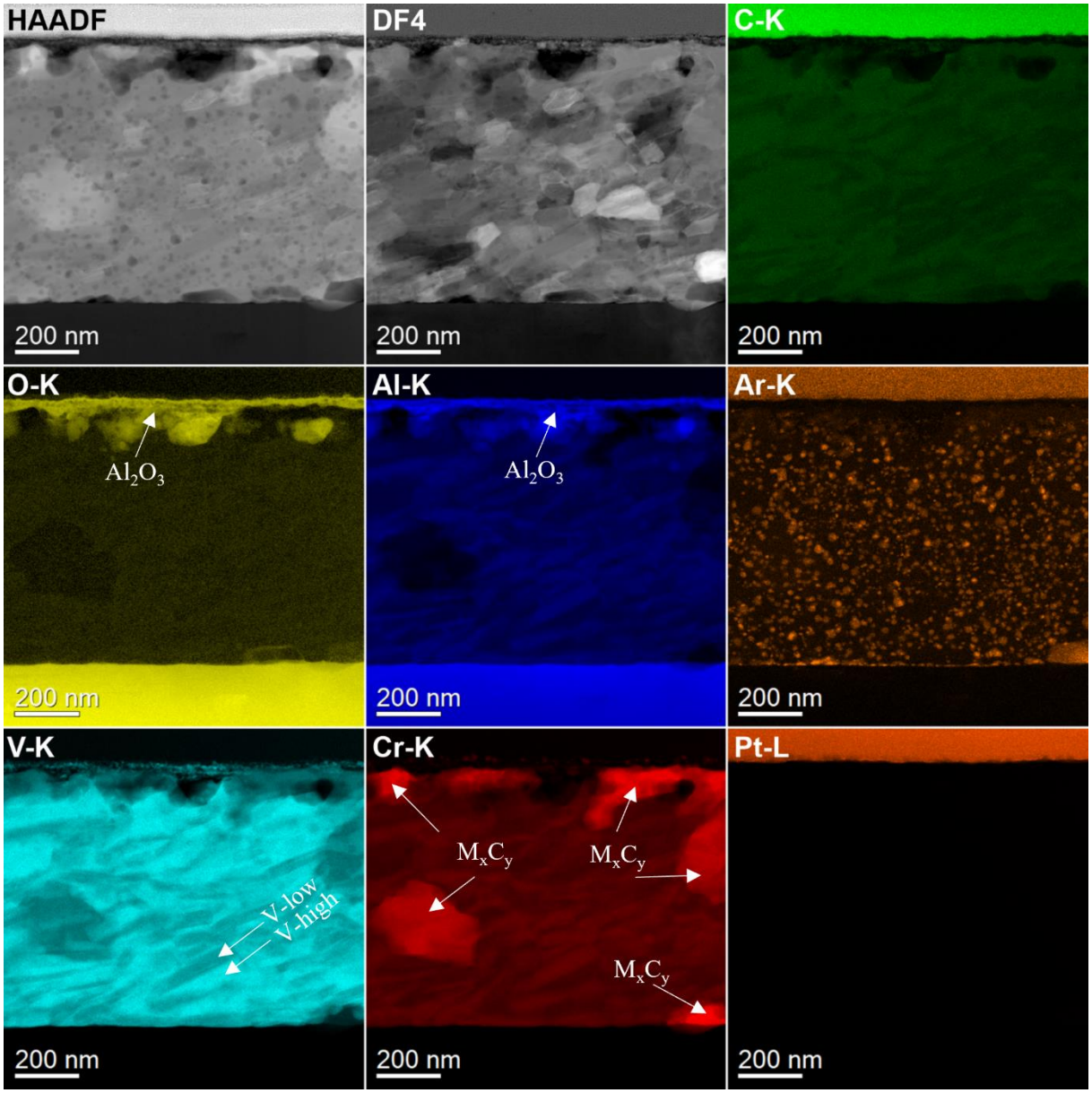

Fig. 9 Cross-sectional TEM analysis of the V-rich thin film sample CrV05 after annealing at 1000°C for 10 min in argon. HAADF-TEM and DF images and results for the EDX-mapping.

Fig. 10 shows a HR-TEM image and associated FFT image highlighting the intergrowth of $(CrV)_2AlC$ and $(CrV)_4AlC_3$ structures within a single grain. The upper part of the grain is identified as $(CrV)_4AlC_3$ and the lower part as $(CrV)_2AlC$. In addition, the two MAX phase structures exhibit coherent interfaces with (0002)[10-10] $(CrV)_2AlC$//(0002)[10-10] $(CrV)_4AlC_3$. Such coherent growth is observed in many individual grains extending over the film thickness. These findings suggest that the lower-ordered 211 MAX phase serves as a template for the crystallization of the higher-ordered 413 MAX phase once appropriate annealing temperature and local composition conditions are met. The epitaxial growth with coherent interface formation obviously reduces the temperature required for crystallization of the higher-ordered

413 MAX phase structure, since synthesis of bulk 413 MAX phases generally requires processing temperature higher than 1500°C [51–53].

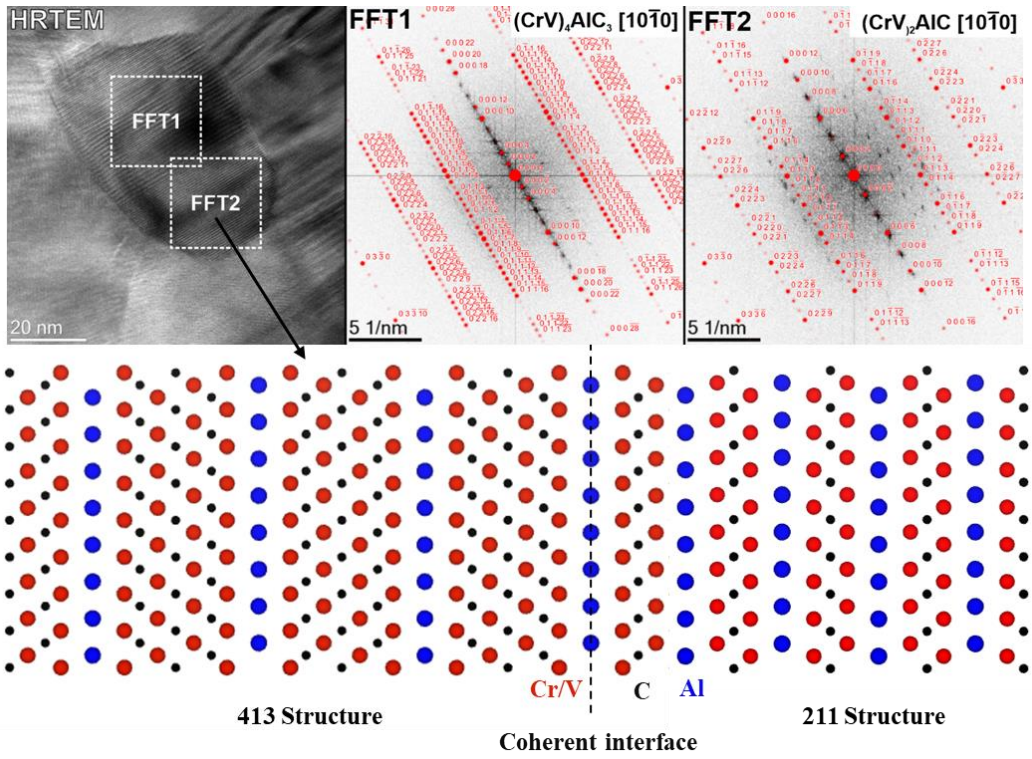

Fig. 10 HRTEM, FFT and schematic images indicating the coherent growth of $(CrV)_4AlC_3$ and $(CrV)_2AlC$ structures in a single grain in the V-rich film CrV05.

Spatially-resolved chemical composition analysis at the nanometer scale of the annealed V-rich CrV05 film studied by atom probe tomography (APT) is presented in Fig.11. The distribution of principal elements (Cr, V, Al, C) apparently shows inhomogeneous features with compositional variations, indicating the growth of different phases. Chemical composition profiles along the cylinder shown in Fig. 11 (b) suggest growth of $(CrV)_2AlC$ and $(CrV)_4AlC_3$ structures without intermediate phases. Combining XRD, HR-TEM and APT analyses, it can be concluded that the nucleation and crystallization of the high-ordered $(CrV)_4AlC_3$ take place via coherent epitaxial growth on the basal plane of $(CrV)_2AlC$. The Cr:V ratios in these two MAX phases derived from APT and TEM analyses are compared in Table 2, and the results are in good agreement. Previous experimental and theoretical studies found that $(CrV)_2AlC$ can exist in the complete Cr:V compositional range, forming solid solutions. Whereas higher-ordered $(CrV)_4AlC_3$ is only stable for vanadium-rich compounds since Cr_4AlC is thermodynamically unstable [9,17]. The $(CrV)_4AlC_3$ phases are clearly vanadium-rich here, with more than 60 at.% V; while Cr and V have nearly equal proportions in the $(CrV)_2AlC$ phases. Some oxygen-rich and Ar-rich clusters were also detected inside the annealed films, with the oxygen signal correlating with pronounced Al content as displayed in Fig. 11 (b). Their formation can

be explained by precipitation of alumina nanograins and growth of nanoscale Ar clusters/bubbles, respectively, during thermal annealing process [26,31].

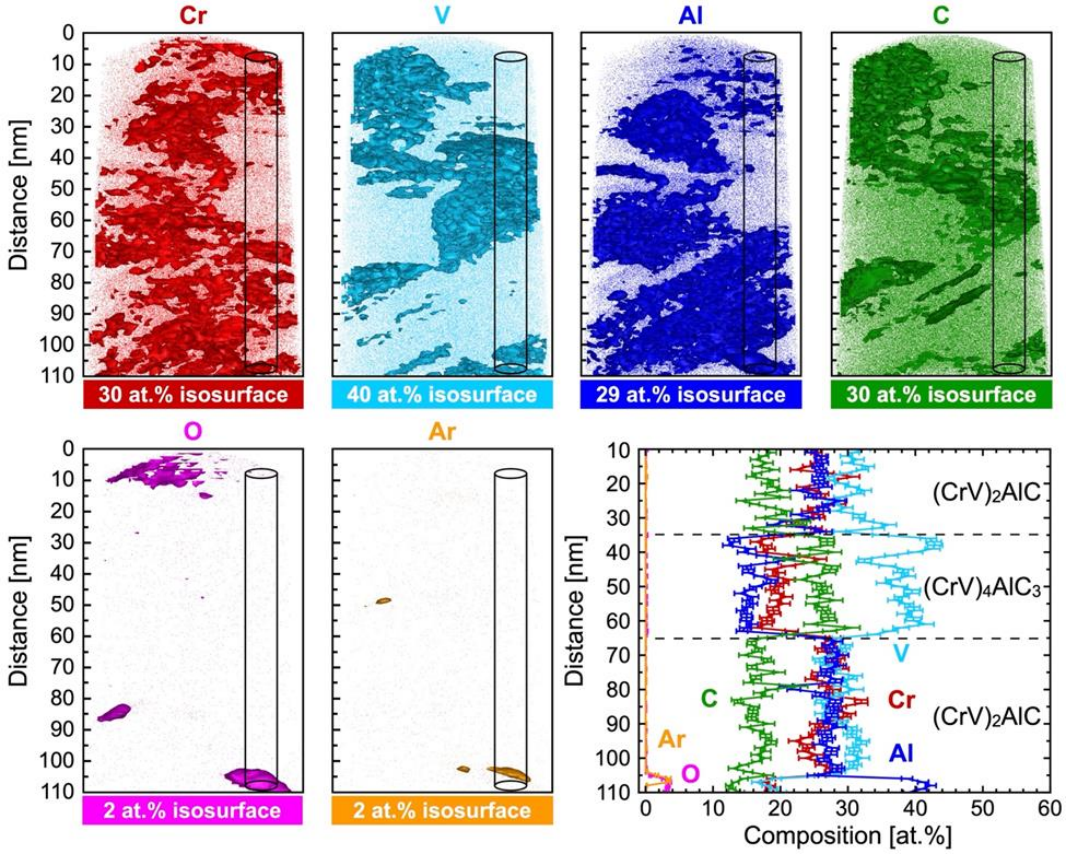

Fig. 11 Local chemical composition analysis of the V-rich film CrV05 after annealing at 1000°C, 10 min in argon by APT. Reconstruction of Cr, V, Al, C, O, and Ar atomic positions with isoconcentration surfaces. The composition profile corresponds to the cylinder region with dimensions of 10 x 10 x 100 nm.

Table 2 Average Cr:V ratio in the two MAX phases of the V-rich film CrV05 determined by APT and TEM.

Phase	Cr:V from APT	Cr:V from TEM
$(CrV)_2AlC$	$Cr_{50}V_{50}$	$Cr_{47}V_{53}$
$(CrV)_4AlC_3$	$Cr_{34}V_{66}$	$Cr_{28}V_{72}$

3.5. Mechanical properties by microindentation

The hardness and reduced Young's modulus determined by microindentation for all multilayered precursors after annealing at 800°C are presented in Fig. 12. All annealed film precursors mainly consist of $(CrV)_2AlC$ MAX phase and some binary secondary phases (Fig. S1), while the higher-ordered $(CrV)_4AlC_3$ MAX phase has not yet formed in the V-rich sample CrV05 since its crystallization temperature is above 900°C. The results provide some insights on the mechanical properties of the $(CrV)_2AlC$ phase with different Cr:V ratios. Their hardness values range from 13.8 to 15.6 GPa, increasing somewhat with increasing V content and then decreasing slightly. The maximum value of the hardness was recorded for CrV04 with 15.6 ± 1.4 GPa. The hardness values obtained here are also consistent with those characteristic of PVD-deposited MAX phase thin films, which are typically several times larger than those of bulk materials due to their nanocrystalline nature and various defects [54,55]. There is no clear trend in the reduced Young's modulus, and their values are comparable, around 280 GPa without strong fluctuation. The reduced Young's modulus measured here is close to the previously reported Young's modulus of its ternary end members [54,56].

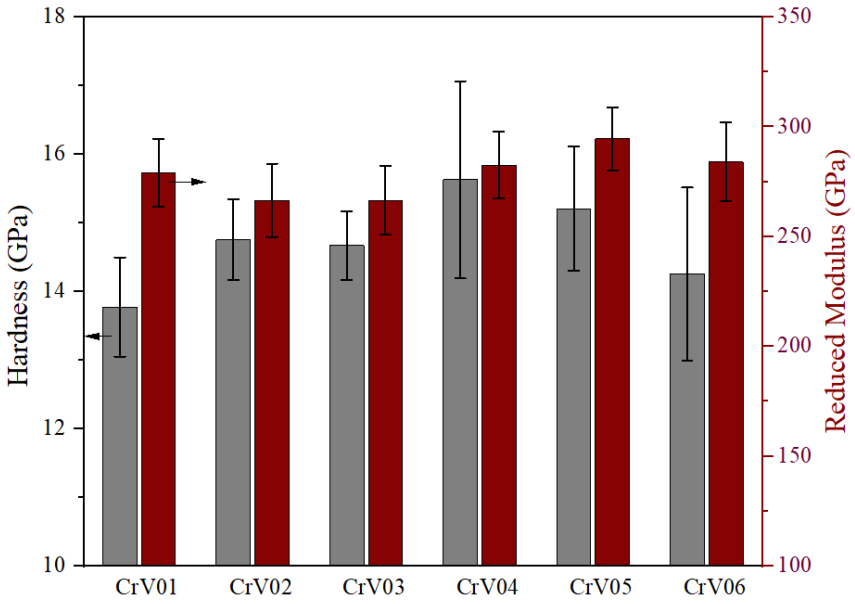

Fig. 12 Hardness and reduced Young modulus of all multilayered precursors after annealing at 800°C, 10 min in argon.

3.6. High-temperature oxidation resistance in steam

The oxidation resistance of three selected films (CrV01, CrV03, and CrV05) with distinct different Cr:V ratios was investigated at 1000°C in steam to explore their oxidative properties and application capability at high temperatures. Their thermally grown oxide scales after oxidation are displayed in Fig. 13 through

cross-sectional SEM images and EDX mapping. It is obvious that the Cr-rich sample CrV01 has not been fully oxidized, while the other two films have been completely oxidized and transformed into oxides. The oxide scale formed on the CrV01 film exhibits a bi-layered structure, as can be seen in Fig. 13 (a). The first, top layer is about 1 µm thick and reveals a porous structure. EDX measurement found that this layer consists of around 30 at.% Al and 10 at.% Cr, and a small amount of V (~ 2 at.%) except O. The second layer beneath this top layer is much thinner, only approximately 0.3 µm, and has a dense structure, primarily composed of Al and O. Therefore, these two oxide sublayers could be categorized as solid solution $(Cr,Al)_2O_3$ and Al_2O_3, respectively. The growth of such bi-layered oxide scale can be explained by the initial oxidation with less protective oxide scales and rapid oxidation kinetics, followed by selective oxidation of Al as the partial pressure of oxidant at the oxide/film interface decreases. The inner dense alumina layer can effectively reduce the diffusion rate of the oxidant and act as an excellent diffusion barrier. As a result, the Cr-rich films exhibit good resistance to oxidation and are not yet fully oxidized. The convoluted interfaces indicate that both inward diffusion of anions and outward diffusion of cations contribute to the oxidation process.

Further increasing the V content from sample CrV01 with composition $Cr_{72.7}V_{27.3}$ to sample CrV03 with composition $Cr_{65.5}V_{34.5}$ likely quickly deteriorate the oxidation resistance of the films. CrV03 and CrV05 films with higher V content cannot establish such bi-layered oxide scale and were completely oxidized, forming one-single layer oxide scale consisting of a mixture of Cr, V, and Al (Fig. 13 (b) and (c)). On the microscopic scale, the three elements are evenly distributed. The oxides identified by XRD analysis (not shown here) were mainly Cr_2O_3 and $VAlO_4$. Previous studies have demonstrated that the V_2AlC MAX phase has poor oxidation resistance in air due to formation of vanadium oxides (mainly VO_2 and V_2O_5) and ternary oxides ($VAlO_4$) at elevated temperatures [57–59]. Selective oxidation of aluminum does not occur in the V_2AlC MAX phase and these vanadium-based oxides cannot effectively protect the underneath materials with high growth rates. Increasing the V concentration beyond 30 at.% of V:(Cr+V) in $(CrV)_2AlC$ may result in incorporation of considerable amount of V into the initially grown oxide scales, which reduces their protective effect and rapidly consumes the entire film. It is worth noting that the lower aluminum content in CrV03 and CrV05 compared to CrV01 may be another reason for their lower oxidation resistance. Overall, the CrV01 films with a V: (Cr+V) ratio of up to ~27 % reveal good oxidation resistance in high-temperature steam. Thus, tailoring the Cr:V ratio in $(CrV)_2AlC$ allows optimizing its specific properties (e.g., oxidation resistance and thermal expansion) to make it chemically and mechanically compatible with different types of substrates for high-temperature application.

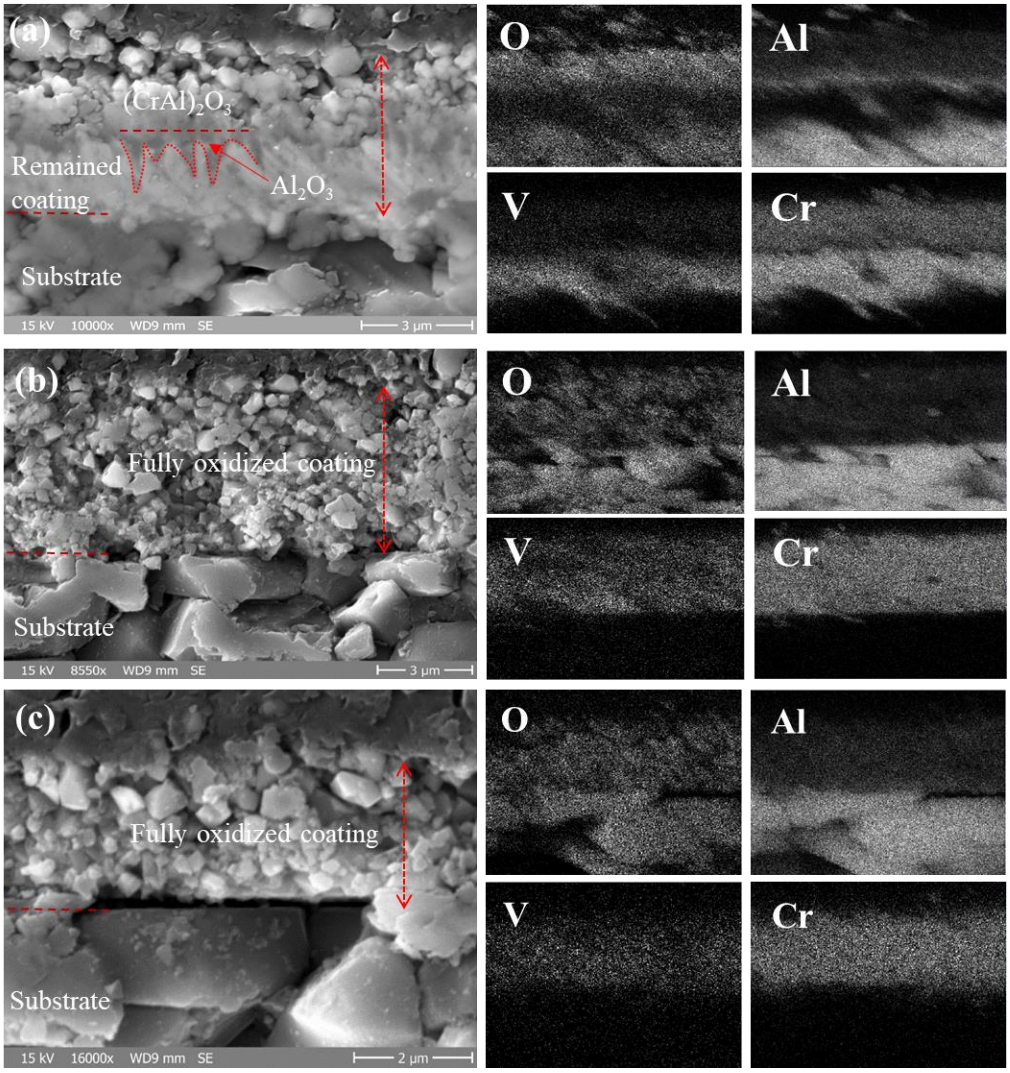

Fig. 13 Cross-section SEM images and EDX mapping of the multilayered precursors CrV01, CrV03 and CrV05 after oxidation at 1000°C in steam for 1 hour.

4. Conclusions

In this study, nanoscale Cr-V/C/Al multilayered precursors with varying Cr:V ratios in the Cr-V sublayers were deposited using magnetron sputtering employing a combinatorial approach. The investigation focused on understanding their phase formation and transformation, microstructure evolution during subsequent thermal annealing aiming to induce crystallization of the solid solution quaternary $(CrV)_{n+1}AlC_n$ MAX phases, along with exploration of selected properties. The key findings and implications derived from this research are summarized as follows:

1. The observed phase transformations and microstructural evolutions of the Cr-V/C/Al multilayered precursors during thermal annealing underscore the dependence on chemical composition, annealing temperature and holding time. Solid solution $(CrV)_2AlC$ MAX phase started to crystallize at around 500°C with disordered $(M,Al)_2C_x$ carbide phase acting as an intermediate product. Growth of higher ordered $(CrV)_4AlC_3$ MAX phase at approximately 960°C was observed in one specific film, suggesting its potential phase stability depending on film stoichiometry and thermal activation.

2. Intriguingly, the nucleation and crystallization of $(CrV)_4AlC_3$ initiate via coherent epitaxial growth on the basal plane of $(CrV)_2AlC$, forming intergrowth structures within one grain. This points to a viable strategy for cultivating the high-ordered $(CrV)_4AlC_3$ MAX phase at reduced processing temperatures, leveraging a lower-ordered 211 MAX phase thin film as a seed layer.

3. $(CrV)_2AlC$ exhibits higher thermal stability than $(CrV)_4AlC_3$ during long-term annealing in an Ar atmosphere at 1200°C, with the decomposition mechanisms primarily linked to the loss of Al atoms. The higher thermal stability of $(CrV)_2AlC$ can be attributed to the higher Al concentration and shorter but stronger Al–M bonds in the 211 structure than those in the 413 structure.

4. Their hardness, measured by microindentation, ranges from 13.8 to 15.6 GPa, comparable to that characteristic of PVD-deposited MAX phase thin films. In terms of oxidation resistance, the findings emphasize the critical role of Cr:V ratios, with the $Cr_{72.7}V_{27.3}$ films exhibiting excellent oxidation performance, forming a bilayer oxide scale of $(Cr,Al)_2O_3$ and Al_2O_3 at 1000°C in steam. However, exceeding this V content compromises oxidation resistance, leading to the growth of a single, mixed oxide layer containing V, Cr, and Al.

The combinatorial synthesis approach serves as a promising strategy for tailoring the design of quaternary solid solution MAX phase thin films and optimizing their associated properties for specific applications by controlling critical parameters such as individual sublayer composition/thickness and interfacial structure in multilayered precursors and thermal processing conditions.

References

[1] M. Schütze, W.J. Quadakkers, Future Directions in the Field of High-Temperature Corrosion Research, Oxid. Met. 87 (2017) 681–704. https://doi.org/10.1007/s11085-017-9719-3.

[2] S. Eswarappa Prameela, T.M. Pollock, D. Raabe, M.A. Meyers, A. Aitkaliyeva, K.L. Chintersingh, Z.C. Cordero, L. Graham-Brady, Materials for extreme environments, Nat. Rev. Mater. 8 (2023) 81–88. https://doi.org/10.1038/s41578-022-00496-z.

[3] J.C. Schuster, H. Nowotny, C. Vaccaro, The ternary systems: CrAlC, VAlC, and TiAlC and the behavior of H-phases (M2AlC), J. Solid State Chem. 32 (1980) 213–219. https://doi.org/10.1016/0022-4596(80)90569-1.

[4] M.W. Barsoum, The MN+1AXN phases: a new class of solids; thermodynamically stable nanolaminates, Prog. Solid State Chem. 28 (2000) 201–281. https://doi.org/10.1016/S0079-6786(00)00006-6.

[5] P. Eklund, M. Beckers, U. Jansson, H. Högberg, L. Hultman, The Mn+1AXn phases: Materials science and thin-film processing, Thin Solid Films 518 (2010) 1851–1878. https://doi.org/10.1016/j.tsf.2009.07.184.

[6] M. Magnuson, M. Mattesini, Chemical bonding and electronic-structure in MAX phases as viewed by X-ray spectroscopy and density functional theory, Thin Solid Films 621 (2017) 108–130. https://doi.org/10.1016/j.tsf.2016.11.005.

[7] Z. Sun, R. Ahuja, S. Li, J.M. Schneider, Structure and bulk modulus of M2AlC (M=Ti, V, and Cr), Appl. Phys. Lett. 83 (2003) 899–901. https://doi.org/10.1063/1.1599038.

[8] M. Sokol, V. Natu, S. Kota, M.W. Barsoum, On the Chemical Diversity of the MAX Phases, Trends Chem. 1 (2019) 210–223. https://doi.org/10.1016/j.trechm.2019.02.016.

[9] M. Dahlqvist, J. Rosen, Predictive theoretical screening of phase stability for chemical order and disorder in quaternary 312 and 413 MAX phases, Nanoscale 12 (2020) 785–794. https://doi.org/10.1039/c9nr08675g.

[10] Y. Li, J. Lu, M. Li, K. Chang, X. Zha, Y. Zhang, K. Chen, P.O.Å. Persson, L. Hultman, P. Eklund, S. Du, J.S. Francisco, Z. Chai, Z. Huang, Q. Huang, Multielemental single–atom-thick A layers in nanolaminated V2(Sn, A) C (A = Fe, Co, Ni, Mn) for tailoring magnetic properties, Proc. Natl. Acad. Sci. 117 (2020) 820–825. https://doi.org/10.1073/pnas.1916256117.

[11] J. Lu, A. Thore, R. Meshkian, Q. Tao, L. Hultman, J. Rosen, Theoretical and Experimental Exploration of a Novel In-Plane Chemically Ordered (Cr2/3M1/3)2AlC i-MAX Phase with M = Sc and y, Cryst. Growth Des. 17 (2017) 5704–5711. https://doi.org/10.1021/acs.cgd.7b00642.

[12] M. Li, J. Lu, K. Luo, Y. Li, K. Chang, K. Chen, J. Zhou, J. Rosen, L. Hultman, P. Eklund, P.O.Å. Persson, S. Du, Z. Chai, Z. Huang, Q. Huang, Element Replacement Approach by Reaction with Lewis Acidic Molten Salts to Synthesize Nanolaminated MAX Phases and MXenes, J. Am. Chem. Soc. 141 (2019) 4730–4737. https://doi.org/10.1021/jacs.9b00574.

[13] B. Tunca, S. Huang, N. Goossens, K. Lambrinou, J. Vleugels, Chemically complex double solid solution MAX phase-based ceramics in the (Ti,Zr,Hf,V,Nb)-(Al,Sn)-C system, Mater. Res. Lett. 10

(2022) 52–61. https://doi.org/10.1080/21663831.2021.2017043.

[14] J. Zhou, Q. Tao, B. Ahmed, J. Palisaitis, I. Persson, J. Halim, M.W. Barsoum, P.O.Å. Persson, J. Rosen, High-Entropy Laminate Metal Carbide (MAX Phase) and Its Two-Dimensional Derivative MXene, Chem. Mater. 34 (2022) 2098–2106. https://doi.org/10.1021/acs.chemmater.1c03348.

[15] A.S. Ingason, M. Dahlqvist, J. Rosen, Magnetic MAX phases from theory and experiments; a review, J. Phys. Condens. Matter 28 (2016) 433003. https://doi.org/10.1088/0953-8984/28/43/433003.

[16] R. Salikhov, A. Mockute, J. Lu, M. Farle, Thin film synthesis and characterization of a chemically ordered magnetic nanolaminate (V,Mn)3GaC2, APL Mater. (2018) 086109. https://doi.org/10.1063/1.4961502.

[17] J. Halim, P. Chartier, T. Basyuk, T. Prikhna, E.N. Caspi, M.W. Barsoum, T. Cabioc'h, Structure and thermal expansion of (Crx,V1-x)n+1AlCn phases measured by X-ray diffraction, J. Eur. Ceram. Soc. 37 (2017) 15–21. https://doi.org/10.1016/j.jeurceramsoc.2016.07.022.

[18] X. Wang, K. Chen, Z. Li, H. Ding, Y. Song, S. Du, MAX phases Hf 2 (Se x S 1 − x) C (x = 0 – 1) and their thermal expansion behaviors, J. Eur. Ceram. Soc. 43 (2023) 1874–1879.

[19] I. Salama, T. El-Raghy, M.W. Barsoum, Oxidation of Nb2AlC and (Ti,Nb)2AlC in Air, J. Electrochem. Soc. 150 (2003) C152. https://doi.org/10.1149/1.1545461.

[20] R. Arróyave, A. Talapatra, T. Duong, W. Son, M. Radovic, Out-of-plane ordering in quaternary MAX alloys: an alloy theoretic perspective, Mater. Res. Lett. 6 (2018) 1–12. https://doi.org/10.1080/21663831.2017.1380723.

[21] Q. Tao, J. Lu, M. Dahlqvist, A. Mockute, S. Calder, A. Petruhins, R. Meshkian, O. Rivin, D. Potashnikov, E.N. Caspi, H. Shaked, A. Hoser, C. Opagiste, R.M. Galera, R. Salikhov, U. Wiedwald, C. Ritter, A.R. Wildes, B. Johansson, L. Hultman, M. Farle, M.W. Barsoum, J. Rosen, Atomically Layered and Ordered Rare-Earth i-MAX Phases: A New Class of Magnetic Quaternary Compounds, Chem. Mater. 31 (2019) 2476–2485. https://doi.org/10.1021/acs.chemmater.8b05298.

[22] H. Fashandi, M. Dahlqvist, J. Lu, J. Palisaitis, S.I. Simak, I.A. Abrikosov, J. Rosen, L. Hultman, M. Andersson, A. Lloyd Spetz, P. Eklund, Synthesis of Ti3AuC2, Ti3Au2C2 and Ti3IrC2 by noble metal substitution reaction in Ti3SiC2 for high-temperature-stable Ohmic contacts to SiC, Nat. Mater. 16 (2017) 814–818. https://doi.org/10.1038/nmat4896.

[23] Y. Zhou, F. Meng, J. Zhang, New MAX-phase compounds in the V-Cr-Al-C system, J. Am. Ceram. Soc. 91 (2008) 1357–1360. https://doi.org/10.1111/j.1551-2916.2008.02279.x.

[24] E.N. Caspi, P. Chartier, F. Porcher, F. Damay, T. Cabioc'h, Ordering of (Cr,V) layers in nanolamellar (Cr0.5V0.5)N+1ALCN compounds, Mater. Res. Lett. 3 (2015) 100–106. https://doi.org/10.1080/21663831.2014.975294.

[25] J. Grossi, S.H. Shah, E. Artacho, P.D. Bristowe, Effect of magnetism and temperature on the stability of (Crx, V1-x)2AlC phases, Phys. Rev. Mater. 2 (2018) 1–8. https://doi.org/10.1103/PhysRevMaterials.2.123603.

[26] X. Chen, B. Stelzer, M. Hans, R. Iskandar, J. Mayer, J.M. Schneider, Enhancing the high temperature oxidation behavior of Cr2AlC coatings by reducing grain boundary nanoporosity,

Mater. Res. Lett. 9 (2021) 127–133. https://doi.org/10.1080/21663831.2020.1854358.

[27] D.E. Hajas, M. to Baben, B. Hallstedt, R. Iskandar, J. Mayer, J.M. Schneider, Oxidation of Cr2AlC coatings in the temperature range of 1230 to 1410°C, Surf. Coatings Technol. 206 (2011) 591–598. https://doi.org/10.1016/j.surfcoat.2011.03.086.

[28] Z. Wang, G. Ma, L. Liu, L. Wang, P. Ke, Q. Xue, A. Wang, High-performance Cr2AlC MAX phase coatings: Oxidation mechanisms in the 900–1100°C temperature range, Corros. Sci. 167 (2020) 108492. https://doi.org/10.1016/j.corsci.2020.108492.

[29] J.E. Yoo, J.Y. Sung, J.H. Hwang, I. Maeng, S.-J. Oh, I. Lee, J.H. Shim, S.D. Kim, D.-S. Yoon, S.Y. Jang, Y.J. Kang, S.W. Lee, MAX-Phase Films Overcome Scaling Limitations to the Resistivity of Metal Thin Films, ACS Appl. Mater. Interfaces 13 (2021) 61809–61817. https://doi.org/10.1021/acsami.1c20516.

[30] T.H. Scabarozi, Combinational investigation of nanolaminate ternary carbie thin films, Drexel University, 2009.

[31] C. Tang, M. Dürrschnabel, U. Jäntsch, M. Klimenkov, M. Steinbrück, S. Ulrich, M. Hans, J.M. Schneider, M. Stüber, Synthesis of V2AlC thin films by thermal annealing of nanoscale elemental multilayered precursors : Incorporation of layered Ar bubbles and impact on microstructure formation, Appl. Surf. Sci. 629 (2023) 157340. https://doi.org/10.1016/j.apsusc.2023.157340.

[32] C. Tang, M. Steinbrück, M. Klimenkov, U. Jäntsch, H.J.H.J. Seifert, S. Ulrich, M. Stüber, Textured growth of polycrystalline MAX phase carbide coatings via thermal annealing of M/C/Al multilayers, J. Vac. Sci. Technol. A 38 (2020) 013401. https://doi.org/10.1116/1.5131544.

[33] T. Gebhardt, D. Music, T. Takahashi, J.M. Schneider, Combinatorial thin film materials science: From alloy discovery and optimization to alloy design, Thin Solid Films 520 (2012) 5491–5499. https://doi.org/10.1016/j.tsf.2012.04.062.

[34] K. Thompson, D. Lawrence, D.J. Larson, J.D. Olson, T.F. Kelly, B. Gorman, In situ site-specific specimen preparation for atom probe tomography, Ultramicroscopy 107 (2007) 131–139. https://doi.org/10.1016/j.ultramic.2006.06.008.

[35] W.C. Oliver, G.M. Pharr, Measurement of hardness and elastic modulus by instrumented indentation: Advances in understanding and refinements to methodology, J. Mater. Res. 19 (2004) 3–20. https://doi.org/10.1557/jmr.2004.19.1.3.

[36] R.A. Baragiola, Sputtering: Survey of observations and derived principles, Philos. Trans. R. Soc. A Math. Phys. Eng. Sci. 362 (2004) 29–53. https://doi.org/10.1098/rsta.2003.1301.

[37] S. Mráz, J. Emmerlich, F. Weyand, J.M. Schneider, Angle-resolved evolution of the composition of Cr-Al-C thin films deposited by sputtering of a compound target, J. Phys. D. Appl. Phys. 46 (2013). https://doi.org/10.1088/0022-3727/46/13/135501.

[38] J.Y. Lee, J.H. Kim, S. Il Park, H.M. Lee, Phase equilibrium of the Ti-Cr-V ternary system in the non-burning β-Ti alloy region, J. Alloys Compd. 291 (1999) 229–238. https://doi.org/10.1016/S0925-8388(99)00144-9.

[39] C. Tang, M. Klimenkov, U. Jaentsch, H. Leiste, M. Rinke, S. Ulrich, M. Steinbrück, H.J. Seifert, M. Stueber, Synthesis and characterization of Ti2AlC coatings by magnetron sputtering from three elemental targets and ex-situ annealing, Surf. Coatings Technol. 309 (2017) 445–455.

https://doi.org/10.1016/j.surfcoat.2016.11.090.

[40] W. Jeitschko, H. Nowotny, F. Benesovsky, Kohlenstoffhaltige ternaire Verbindungen (H-Phase), Monatshefte Für Chemie 94 (1963) 672–676. https://doi.org/10.1007/BF00913068.

[41] B.J. Lee, D.N. Lee, A thermodynamic evaluation of the Fe-Cr-V-C system, J. Phase Equilibria 13 (1992) 349–364. https://doi.org/10.1007/BF02674980.

[42] O. Berger, C. Leyens, S. Heinze, R. Boucher, M. Ruhnow, Characterization of Cr–Al–C and Cr–Al–C–Y films synthesized by High Power Impulse Magnetron Sputtering at a low deposition temperature, Thin Solid Films 580 (2015) 6–11. https://doi.org/10.1016/j.tsf.2015.03.008.

[43] A. Abdulkadhim, M. To Baben, V. Schnabel, M. Hans, N. Thieme, C. Polzer, P. Polcik, J.M. Schneider, Crystallization kinetics of V2AlC, Thin Solid Films 520 (2012) 1930–1933. https://doi.org/10.1016/j.tsf.2011.09.037.

[44] A. Abdulkadhim, M. to Baben, T. Takahashi, V. Schnabel, M. Hans, C. Polzer, P. Polcik, J.M. Schneider, Crystallization kinetics of amorphous Cr2AlC thin films, Surf. Coatings Technol. 206 (2011) 599–603. https://doi.org/10.1016/j.surfcoat.2011.06.003.

[45] J. Emmerlich, D. Music, P. Eklund, O. Wilhelmsson, U. Jansson, J.M. Schneider, H. Högberg, L. Hultman, Thermal stability of Ti3SiC2 thin films, Acta Mater. 55 (2007) 1479–1488. https://doi.org/10.1016/j.actamat.2006.10.010.

[46] I.M. Low, W.K. Pang, Thermal Stability of MAX Phases, Key Eng. Mater. 617 (2014) 153–158. https://doi.org/10.4028/www.scientific.net/KEM.617.153.

[47] I.M. Low, W.K. Pang, S.J. Kennedy, R.I. Smith, High-temperature thermal stability of Ti2AlN and Ti4AlN3: A comparative diffraction study, J. Eur. Ceram. Soc. 31 (2011) 159–166. https://doi.org/10.1016/j.jeurceramsoc.2010.09.014.

[48] C. Tang, M. Steinbrueck, M. Stueber, M. Grosse, X. Yu, S. Ulrich, H.J. Seifert, Deposition, characterization and high-temperature steam oxidation behavior of single-phase Ti2AlC-coated Zircaloy-4, Corros. Sci. 135 (2018) 87–98. https://doi.org/10.1016/j.corsci.2018.02.035.

[49] C. Tang, M. Steinbrück, M. Große, T. Bergfeldt, H.J. Seifert, Oxidation behavior of Ti2AlC in the temperature range of 1400 °C–1600 °C in steam, J. Nucl. Mater. 490 (2017) 130–142. https://doi.org/10.1016/j.jnucmat.2017.03.016.

[50] Z. Liu, J. Yang, H. Zhang, Z. Liu, H. Li, M. Li, Y. Qian, J. Xu, Thermal stability and decomposition behavior of Cr2TiAlC2 at elevated temperature, Ceram. Int. 49 (2023) 12034–12041. https://doi.org/10.1016/j.ceramint.2022.12.053.

[51] M. Hossein-Zadeh, O. Mirzaee, H. Mohammadian-Semnani, An investigation into the microstructure and mechanical properties of V4AlC3 MAX phase prepared by spark plasma sintering, Ceram. Int. 45 (2019) 7446–7457. https://doi.org/10.1016/j.ceramint.2019.01.036.

[52] C. Hu, J. Zhang, J. Wang, F. Li, J. Wang, Y. Zhou, Crystal structure of V4AlC3: A new layered ternary carbide, J. Am. Ceram. Soc. 91 (2008) 636–639. https://doi.org/10.1111/j.1551-2916.2007.02136.x.

[53] J. Etzkorn, M. Ade, H. Hillebrecht, V2AlC, V4AlC3-x (x approximately 0.31), and V12Al3C8: synthesis, crystal growth, structure, and superstructure., Inorg. Chem. 46 (2007) 7646–53.

https://doi.org/10.1021/ic700382y.

[54] D.P. Sigumonrong, J. Zhang, Y. Zhou, D. Music, J.M. Schneider, Synthesis and elastic properties of V2AlC thin films by magnetron sputtering from elemental targets, J. Phys. D. Appl. Phys. 42 (2009) 185408. https://doi.org/10.1088/0022-3727/42/18/185408.

[55] Z. Wang, X. Li, J. Zhou, P. Liu, Q. Huang, P. Ke, A. Wang, Microstructure evolution of V–Al–C coatings synthesized from a V2AlC compound target after vacuum annealing treatment, J. Alloys Compd. 661 (2016) 476–482. https://doi.org/10.1016/j.jallcom.2015.11.170.

[56] M.W. Barsoum, M. Radovic, Elastic and Mechanical Properties of the MAX Phases, Annu. Rev. Mater. Res. 41 (2011) 195–227. https://doi.org/10.1146/annurev-matsci-062910-100448.

[57] C. Azina, S. Mráz, G. Greczynski, M. Hans, D. Primetzhofer, J.M. Schneider, P. Eklund, Oxidation behaviour of V2AlC MAX phase coatings, J. Eur. Ceram. Soc. 40 (2020) 4436–4444. https://doi.org/10.1016/j.jeurceramsoc.2020.05.080.

[58] S. Gupta, M.W. Barsoum, Synthesis and Oxidation of V2AlC and (Ti0.5V0.5)2AlC in Air, J. Electrochem. Soc. 151 (2004) D24–D29. https://doi.org/10.1149/1.1639160.

[59] B. Wang, A. Zhou, Q. Hu, L. Wang, Synthesis and oxidation resistance of V2AlC powders by molten salt method, Int. J. Appl. Ceram. Technol. 14 (2017) 873–879. https://doi.org/10.1111/ijac.12723.

Declaration of Competing Interest

The authors declare that they have no known competing financial interests or personal relationships that could have appeared to influence the work reported in this paper.

Acknowledgements

This work was supported by Deutsche Forschungsgemeinschaft (DFG – German Research Foundation, TA 1693/1- 1). The authors thank colleagues in the Composites and Thin Films Department for technical support.